NASA Public Access
Author manuscript
Nature. Author manuscript; available in PMC 2019 August 08.

Published in final edited form as:
Nature. 2018 August ; 560(7720): 639–643. doi:10.1038/s41586-018-0411-9.

Global land change 1982-2016

Xiao-Peng Song[1,*], **Matthew C. Hansen**[1], **Stephen V. Stehman**[2], **Peter V. Potapov**[1], **Alexandra Tyukavina**[1], **Eric F. Vermote**[3], and **John R. Townshend**[1]

[1]Department of Geographical Sciences, University of Maryland, College Park, MD 20742, USA.

[2]College of Environmental Science and Forestry, State University of New York, Syracuse, NY 13210, USA.

[3]NASA Goddard Space Flight Center, 8800 Greenbelt Road, Greenbelt, MD 20771, USA.

Abstract

Land change is a cause and consequence of global environmental change[1,2]. Land-cover and land-use change significantly alter the Earth's energy balance and biogeochemical cycles, contributing to climate change, which in turn affects land surface properties and the provision of ecosystem services[1–4]. Yet quantification of global land change is lacking. Here, we analyze 35-years of satellite data and provide the first comprehensive record of global land change dynamics during 1982–2016. We show that contrary to the prevailing view that forest area has declined globally[5], tree cover has increased by 2.24 million km^2 (+7.1% relative to 1982 level). This overall net gain is a result of net loss in the tropics outweighed by net gain in the subtropical, temperate and boreal climate zones. Global bare ground cover has decreased by 1.16 million km^2 (−3.1%), most notably in agricultural regions in Asia. Of all land changes, 60% are associated with direct human land-use activities and 40% with indirect drivers such as climate change. Land-use change exhibits strong regional dominance, including tropical deforestation and agricultural expansion, temperate reforestation/afforestation, cropland intensification, and urbanization. Consistent across all climate domains, global montane systems have gained tree cover over the past 35 years, whereas many arid and semi-arid ecosystems have lost vegetation cover. The global land change quantified in our study and the driver attribution results reflect a human-dominated Earth system. The freely available dataset may be used to improve the modeling of land-use change, biogeochemical cycles and vegetation-climate interactions to further advance our understanding of global change[1–4,6].

Humanity depends on land for food, energy, living space and development. Land-use change, a traditionally local-scale human practice, is increasingly affecting Earth system

*Correspondence to: xpsong@umd.edu.

Author contributions: X.P.S. and M.C.H. designed the study; X.P.S. carried out data analysis; X.P.S., M.C.H. and S.V.S wrote the article with contributions from all authors.

Data availability: The generated AVHRR VCF products will be distributed through Land Processes Distributed Active Archive Center (LP DAAC, https://lpdaac.usgs.gov/). VCF change layers are provided at http://glad.geog.umd.edu/dataset/long-term-global-land-change for view and download.

Code availability: The code used for deriving land-cover change from time-series VCF layers is available upon request from the corresponding author.

Competing financial interests: The authors declare no competing financial interests.

Supplementary Information is linked to the online version of the paper at www.nature.com/nature.

NASA Author Manuscript
NASA Author Manuscript
NASA Author Manuscript

NASA Author Manuscript NASA Author Manuscript NASA Author Manuscript

processes, including the surface energy balance, the carbon cycle, the water cycle, and species diversity[1–4]. Land-use change is estimated to contribute a quarter of cumulative carbon emissions to the atmosphere since industrialization[3]. As population and per capita consumption continue to grow, so does demand for food, natural resources and consequent stress to ecosystems. Recent research suggests that human-induced perturbations to the Earth system, especially the climate system, have exceeded natural variability and that we have entered a new geologic epoch referred to as the Anthropocene[7].

Because of their synoptic view and recurrent monitoring of the Earth's surface, satellite observations contribute substantially to our current understanding of the global extent and change of land cover and land use. Previous global-scale studies were mainly focused on annual forest cover change (stand-replacement disturbance) for the time period after 2000[8] or at sparse temporal intervals[9,10]. Long-term gradual changes in undisturbed forests as well as areal changes in cropland, grassland and other non-forested land are less well quantified.

For the time period 1982 to 2016, we create an annual global vegetation continuous fields product[11], consisting of tall vegetation (≥ 5m in height) hereafter referred to as tree canopy (TC) cover, short vegetation (SV) cover and bare ground (BG) cover, at 0.05° × 0.05° spatial resolution (see details of definitions in Methods). For each year, every land pixel is characterized as percent of TC, SV and BG cover, representing the vegetation composition at the time of the local peak growing season. The dataset is produced by combining optical observations from multiple satellite sensors, including the Advanced Very High Resolution Radiometer, the Moderate Resolution Imaging Spectroradiometer, the Landsat Enhanced Thematic Mapper Plus and various very high spatial resolution sensors. We employ non-parametric trend analysis to detect and quantify changes in tree canopy, short vegetation and bare ground over the full time period at pixel (0.05° × 0.05°), regional and global scales. Observed changes are attributed to direct human activities or indirect drivers based on a global probability sample and interpretation of high resolution images from Google Earth.

Total area of tree cover increased by 2.24 million km^2 from 1982 to 2016 (90% confidence interval (CI) [0.93, 3.42] million km^2) representing a +7.1% change relative to 1982 tree cover (Extended Data Table 1). Bare ground area decreased by 1.16 million km^2 (90% CI [−1.78, −0.34] million km^2) representing a decrease of 3.1% relative to 1982 bare ground cover. Area of short vegetation cover decreased by 0.88 million km^2 (90% CI [−2.20, 0.52] million km^2) indicating a decrease of 1.4% relative to 1982 short vegetation cover. A global net gain in tree canopy contradicts current understanding of long-term forest area change; the Food and Agriculture Organization of the United Nations (FAO) reported a net forest loss between 1990 and 2015. However, our gross tree canopy loss estimate (−1.33 million km^2, −4.2%, Extended Data Table 1) agrees, in magnitude, with FAO's net forest area change estimate (−1.29 million km^2, −3%), despite differences in the time period covered and definition of forest (FAO defines forest as tree cover ≥ 10%; see details in Methods).

The mapped land change (Fig. 1) consists of all land-cover and land-use changes induced by natural or anthropogenic drivers. Land-cover and land-use change themes are also inherently linked in the tree cover – short vegetation – bare ground nexus. For example, deforestation for agricultural expansion is often manifested as tree canopy loss and short vegetation gain,

NASA Author Manuscript NASA Author Manuscript NASA Author Manuscript

whereas land degradation may simultaneously result in short vegetation loss and bare ground gain. Pairs of ΔTC, ΔSV and ΔBG show strong coupling and symmetry in change direction but vary substantially over space (Fig. 1b and Extended Data Fig. 1). That is, the globally dominant, coupled land changes are ΔTC co-located with ΔSV and ΔSV co-located with ΔBG.

The overall net gain in tree canopy is a result of net loss in the tropics outweighed by net gain in the subtropical, temperate and boreal climate zones (Extended Data Table 2). A latitudinal north (gain)-south (loss) contrast in tree cover change is evident (Fig. 2a). Conversely, for short vegetation, tropical net gain is exceeded by extratropical net loss. The latitudinal profile of ΔSV largely mirrors that of ΔTC, most obvious in the northern mid-to-high latitudes (45°N-75°N) and low latitudes (30°S-10°N) (Fig. 2b). For bare ground, subtropical net gain partially offsets losses in all other climate domains. In the northern low-to-mid latitudes (10°N-45°N), the profile of bare ground loss (Fig. 2c) closely corresponds to that of short vegetation gain (Fig. 2b).

Changes were unevenly distributed across biomes (Fig. 3, Extended Data Fig. 2 and Extended Data Table 2). The largest area of net tree canopy loss occurred in the tropical dry forest biome (−95,000 km^2, −8%) (Extended Data Fig. 2a), closely followed by tropical moist deciduous forest (−84,000 km^2, −2%) (Fig. 3c) [all percent net changes are expressed relative to the benchmark of the area of the cover class in 1982]. Tree canopy in major forest biomes outside the tropics increased over the past 35 years, with temperate continental forest experiencing the largest gain (+726,000 km^2, +33%) (Fig. 3d), comparable to the next two biomes combined: boreal coniferous forest (+463,000 km^2, +12%) (Extended Data Fig. 2m) and subtropical humid forest (+280,000 km^2, +18%) (Extended Data Fig. 2e).

Short vegetation loss mirrored tree cover gain dynamics, but with smaller magnitudes: temperate continental forest (−610,000 km^2, −14%), boreal coniferous forest (−430,000 km^2, −10%) and subtropical humid forest (−249,000 km^2, −9%). In contrast, tropical forest biomes all gained short vegetation, with tropical shrubland experiencing the largest areal increase (+417,000 km^2, +10%) (Fig. 3e), twice the amount of short vegetation gain in tropical dry forest (+246,000 km^2, +5%). Tropical shrubland also experienced the largest bare ground loss (−408,000 km^2, −10%).

Subtropical desert, the second largest dryland biome on Earth, had the largest gain in bare ground (+154,000 km^2, +4%) (Fig. 3f), followed by subtropical steppe (+107,000 km^2, +5%) (Extended Data Fig. 2h).

Consistent across all climate domains, mountain systems experienced net bare ground loss, net short vegetation loss, and net tree canopy gain (Extended Data Fig. 2c, f, i, n and Extended Data Table 2). In the high-latitude boreal tundra woodland and the polar ecozone (Extended Data Fig. 2o, p), bare ground decreased and tree canopy increased in both biomes, while short vegetation decreased in tundra woodland, but increased in the polar ecozone.

Based on the data from the global probability sample, an estimated 60% of all changes were associated with direct human land-use activities and 40% with indirect drivers such as

NASA Author Manuscript NASA Author Manuscript NASA Author Manuscript

climate change (Extended Data Figs. 3 and 4; see Methods). Direct human impact varied from 36% for bare ground gain to 70% for tree canopy loss. At the continental scale, land-use activities account for the majority of observed land changes in Europe (86%), South America (66%), Asia (62%) and Africa (50%), but play a smaller role in North America (47%) and Oceania (35%). The specific land change drivers are diverse, multi-scale and interactive[1,13] (see below for detailed discussion). However, changes collectively induced by the various drivers at the global scale appear gradual over time (Extended Data Fig. 5).

Expansion of the agricultural frontier is the primary driver of deforestation in the tropics[14]. The three countries with the largest area of net tree cover loss during 1982–2016 are all located in South America: Brazil (−385,000 km^2, −8%), Argentina (−113,000 km^2, −25%) and Paraguay (−79,000 km^2, −34%) (Supplementary Information Table 1). The “arc of deforestation” along the southeastern edge of the Amazon has been well documented[8,9,14,15]. Clearing of natural vegetation for export-oriented industrial agriculture also prevailed in the Cerrado (Fig. 4a) and the Gran Chaco (Fig. 4b). Spatially clustered hotspots of deforestation are also found in Queensland, Australia and Southeast Asia, including Myanmar, Vietnam, Cambodia and Indonesia, diminishing the already scarce primary forests of the region[16]. In sub-Saharan Africa, tree cover loss was pervasive across the Congolian rainforests and the Miombo woodlands (Fig. 4c), historically related to small-holder agriculture, and increasingly for commodity crop cultivation[17]. Forests in boreal Canada, eastern Alaska and central Siberia exhibited large patches of tree canopy loss and short vegetation gain, similar to the tropics (Fig. 1b). However, these are the result of persistent disturbances from wildfires and subsequent recovery of natural vegetation[18].

Discernible impacts of climate change on vegetation change are also revealed at regional scales. In the Western United States (Fig. 4d), forests are suffering from increasing stress from insects, wildfires, heat and droughts due to regional warming[19]. But in the temperature-limited Arctic, warming is facilitating woody vegetation growth in northeastern Siberia, western Alaska and northern Quebec[20] (Fig. 4e). Land-use activities are rare in these boreal tundra and polar ecosystems, contributing less than 1% to observed land changes (Extended Data Fig. 3e). In water-limited savannas in Central and West Africa (Fig. 4f), forest expansion and woody encroachment, observed both from space and in the field[21], are likely driven by increases in precipitation and atmospheric CO_2 [22]. Extreme high rainfall anomalies also contributed to the greening of the Sahel[22] (Fig. 4f). Altitudinal biome shift is also expected in a changing climate. Global treeline positions have been advancing since 1900 AD as a result of climate warming[23]. The aforementioned bare ground loss, short vegetation loss and tree canopy gain in global mountain systems further suggest that an enduring transformation is occurring with regard to the distribution, structure and composition of montane vegetation.

Political, social and economic factors can influence vegetation in conjunction with climate drivers. Tree canopy in Europe, including European Russia, has increased by 35%—the greatest gain among all continents (Extended Data Table 1). Spatially contiguous hotspots of tree canopy gain were found in European Russia and Carpathian montane forests (Fig. 4g). Natural afforestation on abandoned agricultural land is a common process in Eastern Europe after the collapse of the Soviet Union[24]. Our satellite record confirms the effectiveness of

NASA Author Manuscript NASA Author Manuscript NASA Author Manuscript

China's large-scale reforestation and afforestation programs, particularly in the Loess Plateau and the Qin Ling–Daba Mountains[25] (Fig. 4h). Increasing area of plantations in southeastern China has also led to China's tree canopy gain (+34%). Tree canopy also increased in the United States (+15%), mostly in the eastern U.S (Fig. 1b). Unlike declining forest cover in the western U.S. (Fig. 4d), southeastern forests are recovering from historical disturbances or are under intensive forestry management[26].

The world's arid and semi-arid drylands exhibited large areas of decrease in short vegetation and increase in bare ground, indicating long-term land degradation. Hotspots of vegetation loss include southwest U.S., southern Argentina, Kazakhstan, Mongolia (Fig. 4i), Inner Mongolia, China, Afghanistan (Fig. 4j) and large areas of Australia. The decrease of short vegetation cover in eastern Australia is likely the consequence of long-term precipitation decline in the local growing season[27]. Rising surface temperatures, reduction in rainfall, and overgrazing caused extensive grassland deterioration in the Mongolian steppe[28]. A U.S. nationwide ground survey revealed degradation of soils and vegetation along with increased dominance of invasive species in the southwest[29].

Human activities undoubtedly play the dominant role in agricultural and urban landscapes, where lands have been continually modified through human history. India and China had the largest bare ground loss among all countries (India: −270,000 km^2, −34%; China: −250,000 km^2, −7%). India also ranked second in short vegetation gain (+195,000 km^2, +9%), after Brazil (+396,000 km^2, +12%). While the short vegetation gain in Brazil is mainly due to the expansion of agricultural frontiers into natural ecosystems, short vegetation gain in India is primarily due to intensification of existing agricultural lands—a continuation of the "Green Revolution"[30]. Some of the observed bare ground gain can be attributed to resource extraction and urban sprawl, most notably in eastern China (Fig. 4h). However, at the global scale, the growth of urban areas accounts for a small fraction of all land change[31].

Previous studies have found a greening Earth based on trends in satellite-based vegetation properties (e.g. leaf area index or LAI) and have linked the greening trend to a number of climatic and ecological factors[25,32–35]. Recently, using ecosystem models, Zhu *et al.* (2016) attributed 70% of observed global LAI increase to the CO_2 fertilization effect and 4% to land-use change. Our finding that global bare ground cover has decreased over the past 35 years suggests a net increase in vegetation cover and thus agrees with the greening trend. However, our results differ from previous studies by quantifying the prominent role of land use in global vegetation change. Using a global probability-based sample, we attribute 60% of observed land changes to land-use activities (Extended Data Fig. 3). Our empirical approach is based on observations of high-resolution satellite data (Extended Data Fig. 4), avoiding the challenges of modeling the underlying drivers of land change[1,13]. Additionally, our TC-SV-BG land-cover product is thematically more advanced than vegetation indices in characterizing land surface change. For example, differentiating long-term changes in tree cover from other vegetation can facilitate improved understanding of global fluxes of water, carbon and energy[11]. Our study provides observational evidence of increasing tree cover in northern continents, which may constitute the missing carbon sink[3,36]. In contrast, tropical tree cover loss is associated with higher biomass forests and responsible for carbon emissions from deforestation[3,15].

NASA Author Manuscript NASA Author Manuscript NASA Author Manuscript

Results of this study reflect a human-dominated Earth system. Direct human action on landscapes is found over large areas on every continent, from intensification and extensification of agriculture to increases in forestry and urban land uses, with implications for the maintenance of ecosystem services[2]. However, human-induced climate change has been documented as an indirect cause of many of the quantified large-scale regional change dynamics, including woody encroachment in Arctic and montane systems and vegetation loss in semi-arid ecoregions. Continuing land-use change and the increasing role of climate change in modifying land cover warrants continued monitoring of the Earth's land surface from space.

Methods

Definitions

Vegetation continuous fields (VCF) represent land surface as a fractional combination of vegetation functional types that can be remotely sensed from satellites[11]. Consistent with previous research[37–41], the VCF product developed in this study consists of percentages of tree canopy (TC) cover, short vegetation (SV) cover and bare ground (BG) cover. Trees are defined as all vegetation taller than 5 meters in height. TC refers to the proportion of the ground covered by the vertical projection of tree crowns[42,43]. SV characterizes the proportion of the ground covered by vegetation other than trees, including shrubs, herbaceous vegetation, and mosses, while BG represents the proportion of the land surface not covered by vegetation. TC, SV and BG are quantified from nadir view at top of canopy and are mapped during the local annual peak of a growing season[31,41,44]. TC is not equivalent to forest cover, although forest cover may be defined based on TC. For example, the FAO defines forest as a parcel or unit of land of at least 0.5 hectares in size which is covered by 10% or more trees that are 5 meters or taller[5]. Gain or loss in TC, SV, or BG refers to net increase or decrease in each respective cover over the study period due to any anthropogenic or natural factors, excluding temporary changes attributable to within-year vegetation phenology or year-to-year rotations.

Generation of AVHRR VCF

The Advanced Very High Resolution Radiometer (AVHRR) instruments on-board NOAA satellites remain an important data source for studying long-term changes in land surface properties as they provide the longest time-series of global satellite measurements[45–47]. We used the version 4 Long Term Data Record (LTDR) to generate the annual VCF products[47,48]. The LTDR was compiled from AVHRR observations through a series of processing steps including radiometric calibration, geolocation correction, atmospheric correction and bi-directional reflectance effect correction[47]. The daily LTDR surface reflectance data contain 5 multi-spectral layers of AVHRR channels 1–5 and the normalized difference vegetation index (NDVI) layer computed from channels 1 and 2[49]. Each pixel is $0.05° \times 0.05°$ in size. We implemented an improved version of the operational Moderate Resolution Imaging Spectroradiometer Vegetation Continuous Field (MODIS VCF) approach to convert daily LTDR to yearly VCF[38] (Supplementary Information Fig. 1a).

NASA Author Manuscript NASA Author Manuscript NASA Author Manuscript

Daily AVHRR was first aggregated into monthly composites based on the maximum NDVI value in the month. Maximum NDVI composition can minimize cloud contamination, reduce bi-directional and off-nadir viewing effects, minimize band-correlated atmospheric effects and enhance vegetation discrimination[50]. The technique has been widely adopted for generating NDVI and land-cover products from daily satellite data for sensors such as AVHRR, MODIS and VEGETATION[46,51–54].

Monthly composites were subsequently converted to annual phenological metrics[8,38,55–57] (Supplementary Information Fig. 1b). Metrics are statistical transformations of pixel time-series that can capture the salient features of vegetation phenology while maintaining high spatial and temporal data consistency. Metrics thus provide a unique advantage to large-area land cover mapping and monitoring. We created a total of 735 annual metrics from a combination of 5 multi-spectral bands and one NDVI layer, each available as time-series of 12 months.

An empirical normalization procedure was applied to enhance the year-to-year consistency of the AVHRR metrics (Extended Data Fig. 6). Time-series data from AVHRR are known to have systematic discrepancies due to different satellite platforms, orbital drift, changes in sensor design and sensor degradation[45,46,58]. The systematic differences are particularly pronounced before and after year 2000; beginning with NOAA-16 in 2000, satellite orbits were stabilized and a major improvement was introduced in the sensor design to increase sensitivity at the low end of radiance[45]. Research has also shown that the varying observational solar zenith angle as a result of orbital drift affects reflectance more than NDVI and is negatively related to leaf area or positively related to soil exposure[59]. That is, dense vegetation is less affected than sparse vegetation. Additionally, remaining atmospheric effects in the AVHRR surface reflectance can also cause inconsistency between years. The normalization was designed to remove these artifacts unrelated to actual surface change.

A rich literature exists on calibration of AVHRR time series. One commonly used method is to apply calibration coefficients estimated from “stable targets” such as deserts, oceans, clouds or rainforests[60–65]. For example, earlier works by Myneni *et al.*[32,63] used the Sahara desert as reference to adjust global NDVI. Gutman (1999)[64] used global deserts and rainforests to correct reflectances as well as NDVI. Recently, data from well-calibrated sensors such as MODIS and SPOT were used as reference for anchoring AVHRR-based NDVI time series[45,46].

To normalize annual metrics, we designed a two-step approach, using MODIS data as reference. The first step was to apply a dark object subtraction (DOS) to remove systematic biases for vegetated surfaces, especially forest. DOS is also a simple and effective method of removing atmospheric contamination in remotely sensed data[66–70]. We used the intact forest landscapes (IFL)[71] of the tropical rainforest biome (i.e. the minimally disturbed tropical rainforests, average tree cover 97%; Extended Data Fig. 6c) as the dark stable target, which was also considered a spectral end-member. The second step was to apply a slope-based adjustment for pixels that contained visible bare ground. This step involved the use of tropical, subtropical and temperate deserts with 100% Landsat-based bare ground cover[28] (Extended Data Fig. 6c) as the bright stable target, or the other spectral end-member. Biases

NASA Author Manuscript NASA Author Manuscript NASA Author Manuscript

over other land surfaces are assumed to be within these two extreme end members[64]. To create the MODIS reference data, an identical procedure (Supplementary Information Fig. 1a) was applied to daily MODIS LTDR[44] to derive annual metrics for years 2000 through 2016. The 17-year median values for each metric were subsequently derived and used as reference.

DOS was conducted by applying the following equations:

$$y_{m,t,i} = x_{m,t,i} - \bar{B}_{m,IFL} \quad (1)$$

$$\bar{B}_{m,IFL} = \frac{\sum_{j=1}^{n_{IFL}} \left(x_{m,t,j} - r_{m,j} \right)}{n_{IFL}} \quad (2)$$

where, $x_{m,t,i}$ is the original AVHRR value of metric m in year t and pixel i, $y_{m,t,i}$ is the DOS-adjusted AVHRR value, $\bar{B}_{m,IFL}$ is the mean bias of metric m over a total of n_{IFL} IFL pixels indexed by j, $r_{m,j}$ is the MODIS reference value of metric m in IFL pixel j.

The soil-induced bias was then corrected relative to the desert end-member, which has maximum residual bias after DOS correction, as well as the IFL end-member, which has minimum residual bias. Dense vegetation is largely immune to this correction. The correction is summarized by the following equations:

$$z_{m,t,i} = y_{m,t,i} - \bar{B}_{m,DES} * \frac{\left(v_{t,i} - \bar{V}_{t,IFL} \right)}{\left(\bar{V}_{t,DES} - \bar{V}_{t,IFL} \right)} \quad (3)$$

$$\bar{B}_{m,DES} = \frac{\sum_{k=1}^{n_{DES}} \left(y_{m,t,k} - r_{m,k} \right)}{n_{DES}} \quad (4)$$

$$\bar{V}_{t,IFL} = \frac{\sum_{j=1}^{n_{IFL}} v_{t,j}}{n_{IFL}} \quad (5)$$

$$\bar{V}_{t,DES} = \frac{\sum_{k=1}^{n_{DES}} v_{t,k}}{n_{DES}} \quad (6)$$

NASA Author Manuscript NASA Author Manuscript NASA Author Manuscript

where, $z_{m,t,i}$ is the slope-adjusted AVHRR value of metric m in year t and pixel i, $y_{m,t,i}$, is the DOS-adjusted value from equation (1), $\bar{B}_{m,DES}$ is the mean bias of metric m over a total of n_{DES} desert (DES) pixels indexed by k, $v_{t,i}$ is the peak growing season NDVI value of pixel i in year t, $\bar{V}_{t,IFL}$ is the mean peak growing season NDVI value of all IFL pixels, $\bar{V}_{t,DES}$ is the mean peak growing season NDVI value of all desert pixels, and $r_{m,k}$ is the MODIS reference value of metric m in desert pixel k. Here we use peak growing season NDVI, which is one of the metrics and computed as the mean of all NDVI values between 75 and 100 percentiles, in the slope term instead of the annual mean NDVI as used in Gutman (1999)[64], because our annual VCF represents the vegetation state of the local peak growing season. Using this annual metric (before any correction) dynamically optimizes AVHRR data for the growing season of each year.

Adjusted annual metrics were used as input to supervised regression tree models to generate the annual TC and BG product. This non-parametric machine learning method was chosen as it can accommodate nonlinear relationships between the dependent variable (percent TC or percent BG) and independent variables (AVHRR metrics); in addition, the decision rules are easily interpretable[72–74]. Training data for TC were obtained by spatially aggregating the circa-2000 Landsat-based percent TC product from 0.00025° × 0.00025° to 0.05° × 0.05°, which was in turn trained using very-high spatial resolution images[8]. For each 0.05° × 0.05° grid cell, we computed the average value of all Landsat TC pixels that fall in the grid cell and derived the percentage of TC per grid cell. Likewise, training data for BG were obtained by spatially aggregating the circa-2000 Landsat-based percent BG product[31]. Model training and prediction were performed separately for TC and BG. We pooled two years of AVHRR metrics before and after 2000 (i.e. 1999 and 2001) as input features to train 21 bagged regression tree models to account for the remaining inter-annual bias of AVHRR metrics, if any, as well as to avoid over-fitting of the regression tree algorithm. The 21 trained models were applied to annual AVHRR metrics to generate percent TC and BG for each year. Due to missing data in years 1994 and 2000, TC and BG maps in these two years were not produced from AVHRR, but were linearly interpolated using antecedent and subsequent annual TC or BG estimates on a per pixel basis. Following the MODIS VCF approach[38], annual SV was derived as the residual term by subtracting TC and BG percentages from 100. Permanent water surfaces were excluded based on the Landsat-derived permanent surface water product[8].

Accuracy assessment

Validating a global land-cover product spanning multiple decades is a challenge. The primary obstacle is the lack of sufficient ground observations that match the spatial extent, the temporal frequency and the thematic content of a satellite-derived product. Satellite observations with higher spatial and temporal resolutions can characterize land cover and change with higher accuracy[75]. Thus, higher-resolution satellite or aerial imagery is often employed to replace ground observations when determining the reference condition for validation[76]. Here we leverage the established validation protocols[77,78] and the best available reference datasets to evaluate the accuracy of our VCF product. Specifically, we used a sub-meter resolution, global land-cover validation sample developed by the United

NASA Author Manuscript NASA Author Manuscript NASA Author Manuscript

States Geological Survey (USGS)[79] as the primary reference for TC. We also used the 30-m resolution Landsat-based TC, SV and BG estimates as reference to evaluate the AVHRR-derived TC, SV and BG layers.

The USGS reference dataset is a stratified random sample of TC estimates produced from n = 475 sample blocks distributed across the globe[77–79] (Extended Data Fig. 7a). Each sample block was 5-km × 5-km (~0.05° × 0.05°) in size. Sub-meter resolution commercial images including QuickBird, WorldView, IKONOS and GeoEye between years 2002 and 2014, depending on each block, were classified to categorical land cover classes including tree cover[79]. The percent TC for each block was computed from these data to provide the reference values for comparison to the AVHRR percent TC. The USGS reference data were developed in Universal Transverse Mercator (UTM) projection and the footprints of the 5-km × 5-km reference sample blocks did not exactly overlap with AVHRR pixels, which were in Geographical Latitude / Longitude projection (Extended Data Fig. 7b-c). This geolocation mismatch inevitably introduced some error in the validation results. Thus, we also evaluated AVHRR TC using the Landsat-based TC estimates. Because the spatial units of the Landsat estimates were spatially aligned with the AVHRR pixels, this comparison is free from geolocation error. For BG and SV, due to the lack of reliable high-resolution reference data, we used Landsat-based BG and SV (computed as 100% – Landsat-based BG% – Landsat-based TC%) estimates at the USGS sample locations as reference data for estimating accuracy. These BG and SV reference data were obtained for the same stratified sample of blocks used to evaluate the AVHRR TC product[77,78].

The paired AVHRR and reference VCF values were used to calculate four accuracy metrics including root-mean-square-error (RMSE), mean absolute error (MAE), mean error (ME) and r^2 [78,80]:

$$RMSE = \sqrt{\frac{\sum_{i=1}^{n} w_i * (p_i - r_i)^2}{\sum_{i=1}^{n} w_i}} \quad (7)$$

$$MAE = \frac{\sum_{i=1}^{n} w_i * |p_i - r_i|}{\sum_{i=1}^{n} w_i} \quad (8)$$

$$ME = \frac{\sum_{i=1}^{n} w_i * (p_i - r_i)}{\sum_{i=1}^{n} w_i} \quad (9)$$

NASA Author Manuscript NASA Author Manuscript NASA Author Manuscript

$$r^2 = 1 - \frac{\sum_{i=1}^{n}(p_i - r_i)^2}{\sum_{i=1}^{n}(p_i - \bar{r})} \quad (10)$$

where p_i, r_i and w_i are estimated VCF, reference VCF and sample weight (inverse of inclusion probability of the sample block for the stratified design) at a location i in a sample of size n; $\bar{r}$ is the estimated mean of the reference values.

We also computed the conventional confusion matrices including overall accuracy (OA), user's accuracy (UA) and producer's accuracy (PA) using the paired AVHRR and reference VCF values and a general ratio estimator[78,81]:

$$\hat{R} = \frac{\sum_{h=1}^{H} N_h * \bar{y}_h}{\sum_{h=1}^{H} N_h * \bar{x}_h} \quad (11)$$

where, H is the total number of strata; N_h is the total number of 5-km × 5-km blocks within stratum h; $\bar{y}_h$ and $\bar{x}_h$ are the sample means of variables y and x in stratum h and the specific identity of y and x depends on the accuracy metric being estimated. To estimate OA, y = area of agreement between AVHRR and reference for a VCF class c in each sample block (i.e., overlapped area) and x = area of the sample block. To estimate UA, y = area of agreement between AVHRR and reference for a VCF class c and x = area of class c mapped by AVHRR. To estimate PA, y = area of agreement between AVHRR and reference for a VCF class c and x = area of class c given by reference.

The estimated variance of $\hat{R}$ is:

$$\hat{V}(\hat{R}) = \frac{1}{\hat{X}^2}\sum_{h=1}^{H} N_h^2(1 - n_h/N_h)\left(s_{yh}^2 + \hat{R}^2 * s_{xh}^2 - 2 * \hat{R} * s_{xyh}\right)/n_h \quad (12)$$

where $\hat{X}^2 = \sum_{h=1}^{H} N_h * \bar{x}_h$, n_h is the number of sample blocks selected from stratum h, s_{yh}^2 and s_{xh}^2 are the sample variances of y and x for stratum h and s_{xyh} is the sample covariance of x and y for stratum h. The standard error of $\hat{R}$ is the square root of the estimated variance. As noted above, the identity of x and y depends on the accuracy metric being estimated. A summary of accuracy results for TC, SV and BG is provided in Extended Data Fig. 7.

Trend analysis

Per-pixel TC, SV and BG percentages were aggregated to a series of spatial scales including global, continental, climate zone, biome and country scales to obtain annual total area estimates at these aggregated scales. For example, for the trend analysis of Africa, the per-pixel values of each cover type were aggregated to produce a single value for each year in the time series. We used the FAO ecological zones boundary shapefile to report VCF area

NASA Author Manuscript NASA Author Manuscript NASA Author Manuscript

estimates per biome and per climate zone[12]. We also used the Global Administrative Areas (GADM) country boundary shapefile (http://www.gadm.org) to report VCF area estimates per country.

The approach to change analysis was predicated on using a linear trend (Theil-Sen estimator) to smooth the annual time series of data when determining net change[82]. Although the classification methodology (monthly compositing, annual metrics calculation, inter-annual bias adjustment and multi-year model training) was constructed to ensure year-to-year consistency to the degree possible, the smoothing approach was still necessary because of the annual variation in the percent TC, SV, and BG values attributable to a variety of sources including different weather conditions, varying vegetation phenology, and image misregistration. For TC, SV and BG time series in each aggregated spatial unit (e.g., a biome or a country), we applied the Theil-Sen estimator to derive the slope (annual change) of trend and provide the estimate of net change between 1982 and 2016 (i.e., slope times 34 years). The upper and lower change estimates based on the 90% confidence interval for the slope were also derived (Extended Data Tables 1 and 2, Supplementary Information Table 1). It is important to point out that the derived Theil-Sen trend represents long-term land-cover changes as the effect of changes in sensor capabilities has been effectively removed.

We further imposed the objective constraint of statistical significance of the trend to define net change at the pixel level. A Mann-Kendall test was applied to the TC, SV, and BG time series in each pixel[83]. If the Mann-Kendall test was not statistically significant ($p \geq 0.05$), we defined net change as 0. If the trend test was significant ($p < 0.05$), we applied the Theil-Sen estimator to estimate the per-pixel net change between 1982 and 2016. These non-parametric statistical methods were chosen due to their robustness for trend detection and insensitivity to outliers. They have been applied to detect the greenness trend of land surface using AVHRR-based NDVI and leaf area index datasets[34,84,85] as well as the microwave-based vegetation optical depth data[86]. Six global VCF gain (positive slope) and loss (negative slope) layers were derived: (i) tree canopy gain; (ii) tree canopy loss; (iii) short vegetation gain; (iv) short vegetation loss; (v) bare ground gain; and (vi) bare ground loss (Fig. 1b and Extended Data Fig. 1). Subsequently, per-pixel loss (gain) were aggregated to global, continental, climate zone, biome and country scales to derive gross loss (gain) estimates for each aggregated spatial unit (Extended Data Tables 1 and 2, Supplementary Information Table 1).

Driver attribution

Drivers of land-cover and land-use change are diverse, multi-scale and interactive[1,13,87–89]. Different drivers can be most broadly classified into two groups: anthropogenic and natural. Anthropogenic drivers are mainly related to land-use activities (e.g., deforestation, agricultural expansion, agricultural intensification, infrastructure construction and resource extraction), which are in turn driven by a number of underlying demographic, economic, technological, institutional, and cultural factors. Natural land-change drivers also include a variety of agents such as wildfire, drought, flood, windthrow, landslide, disease, insect attack, natural vegetation growth and glacial retreat, many of which are related to long-term climatic variation. Different drivers interact with each other in complex ways and the

NASA Author Manuscript NASA Author Manuscript NASA Author Manuscript

interactions are even evident at the broadest level in the Anthropocene[7]. With substantial human perturbations to the climate system, human-induced climate change and natural climatic variation and their effect on terrestrial ecosystems are intertwined. Disentangling human-induced climate change from natural climatic variation is a challenge, which can be studied using Earth system models[35]. Our objective for the global driver attribution was to provide a statistical, observation-based estimate of the relative contribution of direct human activities versus indirect drivers (including the combined effects of natural and human-induced climate change) to the observed global land change. Regionally dominant, specific land-change drivers were not explicitly quantified, but were identified and summarized through a comprehensive literature review.

We used a global probability sample and interpretation of high resolution images from Google Earth to estimate the proportion of changes attributable to drivers[90,91], separately for each VCF change type: (i) tree canopy gain; (ii) tree canopy loss; (iii) short vegetation gain; (iv) short vegetation loss; (v) bare ground gain; and (vi) bare ground loss. For each VCF change type, 250 sample pixels (a pixel is a 0.05° × 0.05° grid cell) were selected with probability proportional to each pixel's absolute change area (−1 * change area in the case of loss) of the target VCF change type, where the area of change was obtained from the global change layers described above. A total of 1500 sample pixels were selected (Extended Data Fig. 3a). For each sample pixel, we created a polygon feature representing its boundary and imported it in Google Earth (Extended Data Fig. 4). Each polygon was also divided into 25 0.01° × 0.01° grid cells to aid photo interpretation (Extended Data Fig. 3b-h). We used high-resolution images and the time slider tool in Google Earth to estimate the proportion of a pixel under human land use, including forestry and agricultural landscapes, cities, villages, houses, roads and other artificial objects. This proportion value was defined as the direct human impact associated with land-cover and land-use changes within the pixel. The impact of indirect drivers was defined as the residual of direct human impact. Areas of long-term land degradation resulting from the combined effects of land use and climate change were labeled as indirect if no signs of land use, for example fence lines or grazing paddocks, were observed. We estimated the direct human impact for each VCF change type as well as all land changes, using the following equations:

$$H_c = \frac{\sum_{j=1}^{n_c} h_j}{n_c} \quad (13)$$

$$OH = \frac{\sum_{c=1}^{6} w_c * H_c}{\sum_{c=1}^{6} w_c} \quad (14)$$

where H_c is the direct human impact of each of the 6 cover change types indexed by c, h_j is the proportion of pixel j that is under human land use, n_c is sample size (n_c= 250), OH is the overall direct human impact of all land changes, and w_c is the weight of each cover change type, given by the proportion of its global area over total absolute change area of all types

NASA Author Manuscript

NASA Author Manuscript

NASA Author Manuscript

(Extended Data Table 1). Similarly, we also estimated the overall direct human impact for all land changes within a continent and a biome. Attribution results are summarized in Extended Data Fig. 3.

Uncertainty analysis

The uncertainties of the area estimates of net land-cover change were characterized as statistical bounds (Extended Data Tables 1 and 2). Here we conducted an additional uncertainty analysis on gross change estimates to investigate whether the overall VCF trends hold true.

We first varied the statistical significance level in the Mann-Kendall trend test for defining change. Compared with change area estimates resulted from the $p < 0.05$ threshold, using $p < 0.1$ to define change, the estimated TC, BG and SV change area would differ by 6%, 2% and 14% respectively, whereas using $p < 0.01$ to define change, the estimated TC, BG and SV change area would differ by 16%, 1% and 31% respectively. Moreover, the signs of TC, BG and SV change were consistent at all significance levels — net gain in TC, net loss in BG and net loss in SV.

We further investigated the effect of VCF mapping uncertainty on change characterization. We employed the deviance value (i.e., the sum of squared difference between predicted value and training reference value) of each leaf node of the bagged regression tree models and computed a root-mean-square-deviation (RMSD) layer as VCF prediction uncertainty[72,92]. This per-pixel uncertainty layer was produced for each year between 1982 and 2016. Since RMSD is a quantitative indicator of land-cover uncertainty, we compared it with the magnitude of land-cover change by constructing a “signal-to-noise” ratio. The uncertainty of change for a given pixel i is then represented by the ratio of land-cover change to RMSD, summarized using the following equations:

$$\overline{RMSD}_i = \frac{\sum_{k=1}^{N} RMSD_{i,k}}{N} \quad (15)$$

$$r_i = \frac{\Delta VCF_i}{\overline{RMSD}_i} \quad (16)$$

where, for each pixel i in year k, the annual mean $\overline{RMSD}_i$ (unit: percent land cover) is the average value of N years; the ratio metric r_i for each pixel i is computed as 1982–2016 VCF change within the pixel (ΔVCF_i in units of percent land cover) to 1982–2016 average model prediction uncertainty $\overline{RMSD}_i$.

A greater absolute value of the ratio metric r_i indicates lower uncertainty of land-cover change and vice versa (Extended Data Figure 8). The density distributions (Extended Data Fig. 8c and 8d) suggest that for any threshold (dashed lines), the proportion of area under the

NASA Author Manuscript

NASA Author Manuscript

NASA Author Manuscript

frequency curve for tree cover gain always exceeds tree cover loss and similarly the proportion of area under the frequency curve for bare ground loss always exceeds bare ground cover gain. Hence, the overall trends in r_i corroborate the main findings of our study, which are that there is a net gain in tree cover and a net loss in bare ground cover over the study period of 1982 to 2016.

Extended Data

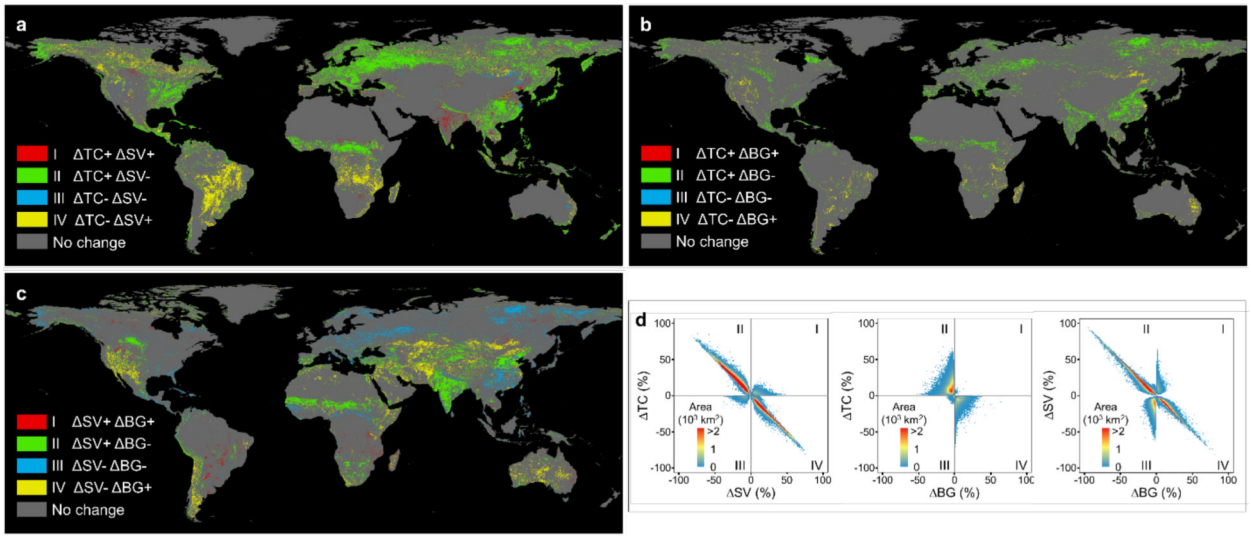

Extended Data Figure 1.

Satellite-derived, long-term (1982–2016) tree canopy cover change (ΔTC), short vegetation cover change (ΔSV) and bare ground cover change (ΔBG) show strong coupling and symmetry in change detection. **a,** Global map of co-located ΔTC and ΔSV. Pixels showing a statistically significant trend (Mann-Kendall test, $p < 0.05$) in both TC and SV are depicted on the map. **b,** Global map of co-located ΔTC and ΔBG. **c,** Global map of co-located ΔSV and ΔBG. **d,** From left to right, intensity plot of change area for ΔTC vs. ΔSV, ΔTC vs. ΔBG and ΔSV vs. ΔBG, corresponding to **a**, **b** and **c** respectively. To create these intensity plots, paired percent change layers (Fig. 1b) are used to construct a 2D histogram with bin size of 1% for both axes. Then, the total change area in each bin is calculated and plotted.

NASA Author Manuscript

NASA Author Manuscript

NASA Author Manuscript

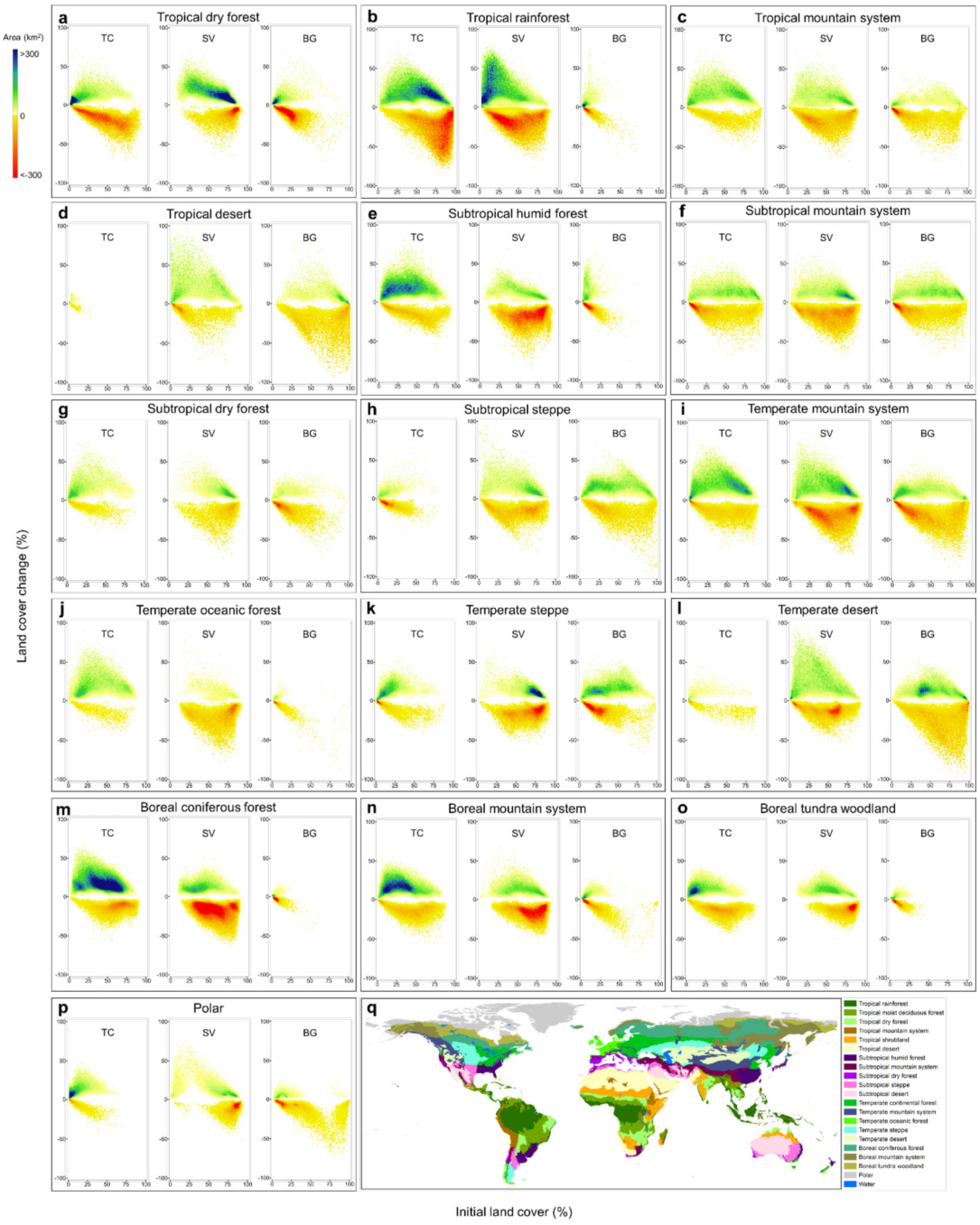

Extended Data Figure 2.

Long-term (1982–2016) gross change dynamics of tree canopy (TC) cover, short vegetation (SV) cover and bare ground (BG) cover vary considerably between biomes (**a-p)**. Mountain systems (**c, f, i, n**) all exhibit larger area of TC gain than TC loss, larger area of SV loss than SV gain and larger area of BG loss than BG gain. **q,** Geographical distribution of all biomes[12]. See Extended Data Table 2 for change area estimates.

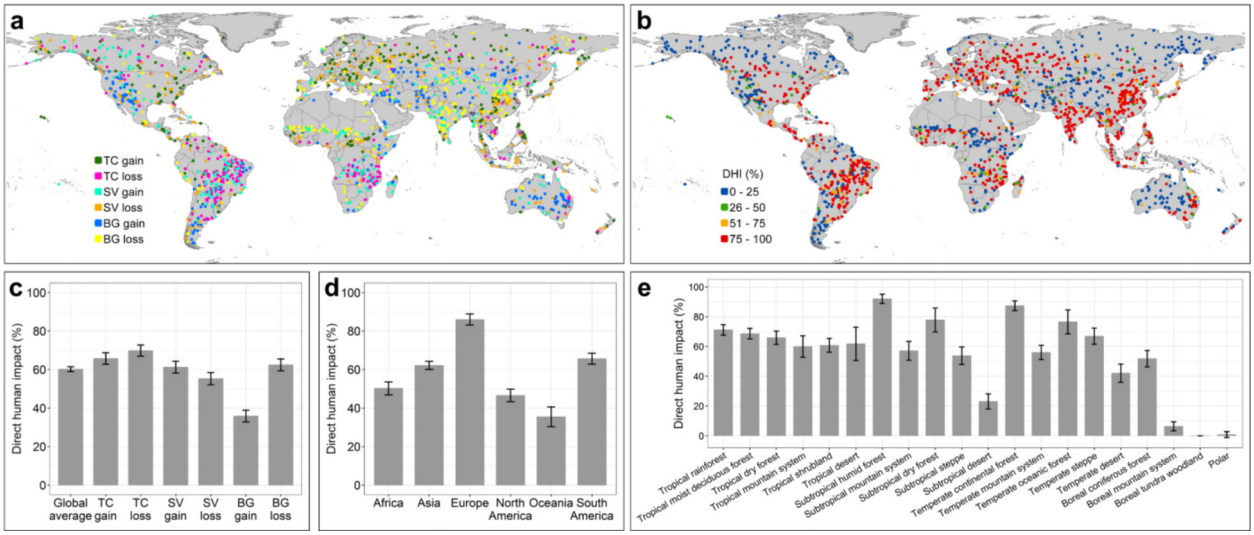

Extended Data Figure 3.

Attributing direct human impact (DHI) versus indirect drivers to detected tree canopy (TC) cover change, short vegetation (SV) cover change, and bare ground (BG) cover change. Indirect drivers include both natural drivers and human-induced climate change. **a,** Spatial distribution of the probability sample used for the attribution estimates (n = 1500). **b,** DHI of each sample unit interpreted using a time-series of high resolution images in Google Earth. **c,** Estimated direct human impact at the global scale. Global average is calculated by weighting the human impact of each type by each respective global total area provided in Extended Data Table 1. Error bars represent the standard error (SE) for the estimated percent of direct human impact. **d** and **e,** Estimated direct human impact at the continental and biome scales.

NASA Author Manuscript NASA Author Manuscript NASA Author Manuscript

NASA Author Manuscript
NASA Author Manuscript
NASA Author Manuscript

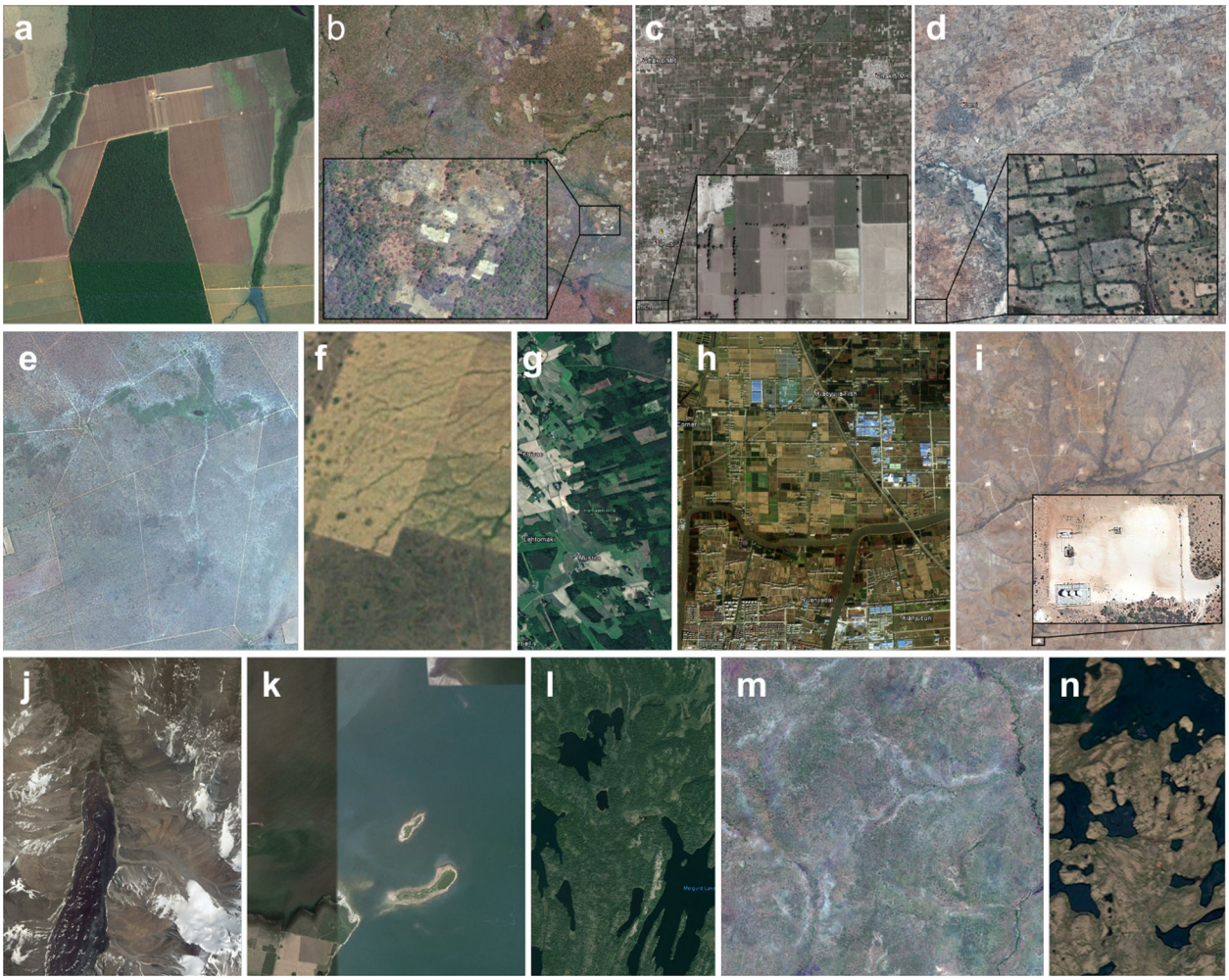

Extended Data Figure 4.

Selected sample examples for driver attribution. Screenshots are taken from Google Earth. Each panel is 0.05° × 0.05° in size, corresponding to one AVHRR pixel. **a**, Deforestation for industrial agriculture expansion in Mato Grosso, Brazil (11.275°S, 52.125°W); **b**, Expanding shifting agriculture in northern Zambia (11.625°S, 28.625°E) **c**, Intensification of small-holder agriculture in Punjab, Pakistan (30.025°N, 71.675°E); **d**, Short vegetation gain in low-intensity agricultural lands in northern Nigeria (12.825°N, 7.825°E), **e**, Short vegetation increase due to effective fire suppression in pasture lands in Omaheke, Namibia[93] (22.175°S, 18.925°E); **f**, Managed pasture lands in western Kazakhstan (49.475°N, 47.725°E), **g**, Forestry in southern Finland (61.075°N, 24.475°E), **h**, Urbanization in Shanghai, China (30.925°N, 121.175°E). **i**, Oil extraction in New Mexico, USA (32.875°N, 104.275°W). **j**, Herbaceous vegetation increase due to glacial retreat in Chuy, Kyrgyzstan (42.575°N, 74.775°E); **k**, Bare ground cover variation along Mar Chiquita lake shore in Cordoba, Argentina (30.675°S, 63.025°W). **l**, Forest fires in Saskatchewan, Canada (55.225°N, 102.225°W); **m**, Tree cover increase in unpopulated savannas in Western Equatoria, South Sudan[21,22] (6.575°N, 27.725°E); **n**, Climate change-driven woody encroachment in Quebec,

NASA Author Manuscript NASA Author Manuscript NASA Author Manuscript

Canada[20] (59.475°N, 73.225°W). Examples **a-i** show various types of land use, whereas examples **j-n** do not show visible signs of human activity.

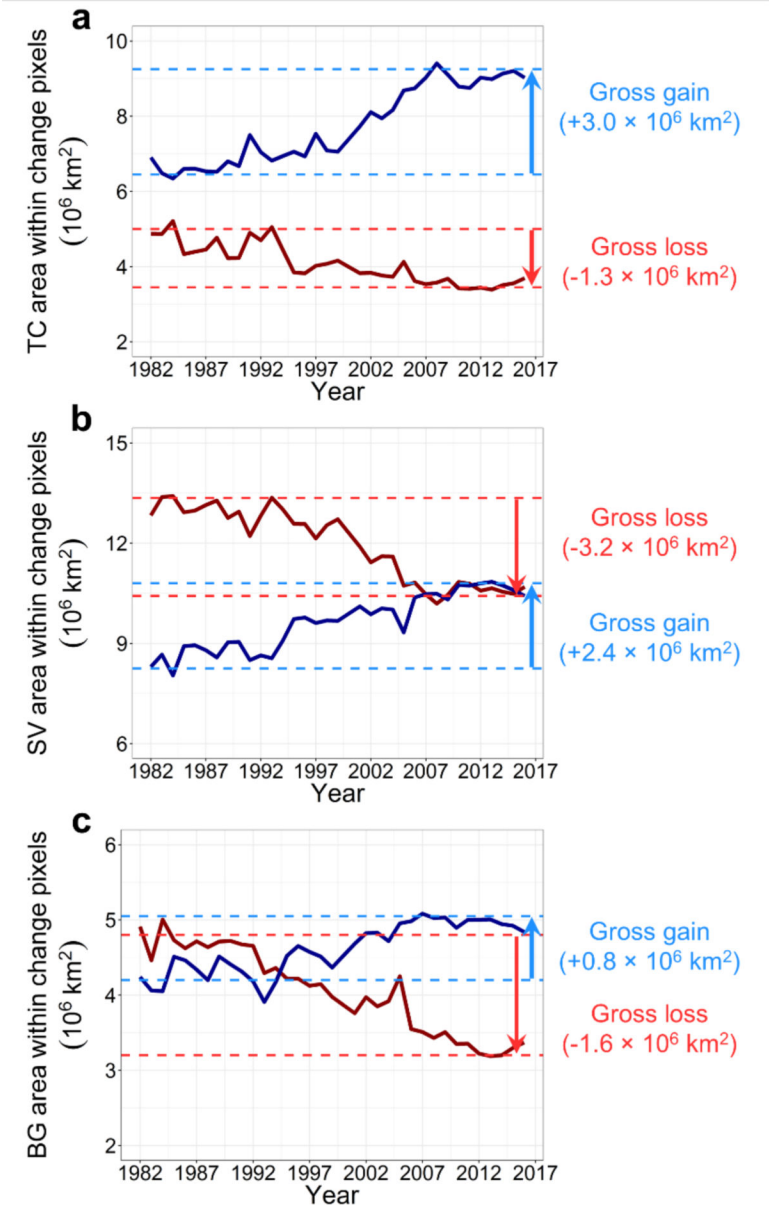

Extended Data Figure 5.

Global trends in (**a**) tree canopy (TC) cover, (**b**) short vegetation (SV) cover, and (**c**) bare-ground (BG) cover during 1982–2016. The following steps were taken for each cover type using TC as the example. The TC gain layer (Fig. 1b) was overlaid on the annual TC% stack to compute annual global TC area within the gain mask (solid dark blue lines); the TC loss layer (Fig. 1b) was overlaid on the annual TC% stack to compute annual global TC area within the loss mask (solid dark red lines). Gross gain (loss) estimates between 1986 and 2016 are marked by blue (red) arrows and dashed lines. See Extended Data Table 1 for exact gross change estimates.

NASA Author Manuscript NASA Author Manuscript NASA Author Manuscript

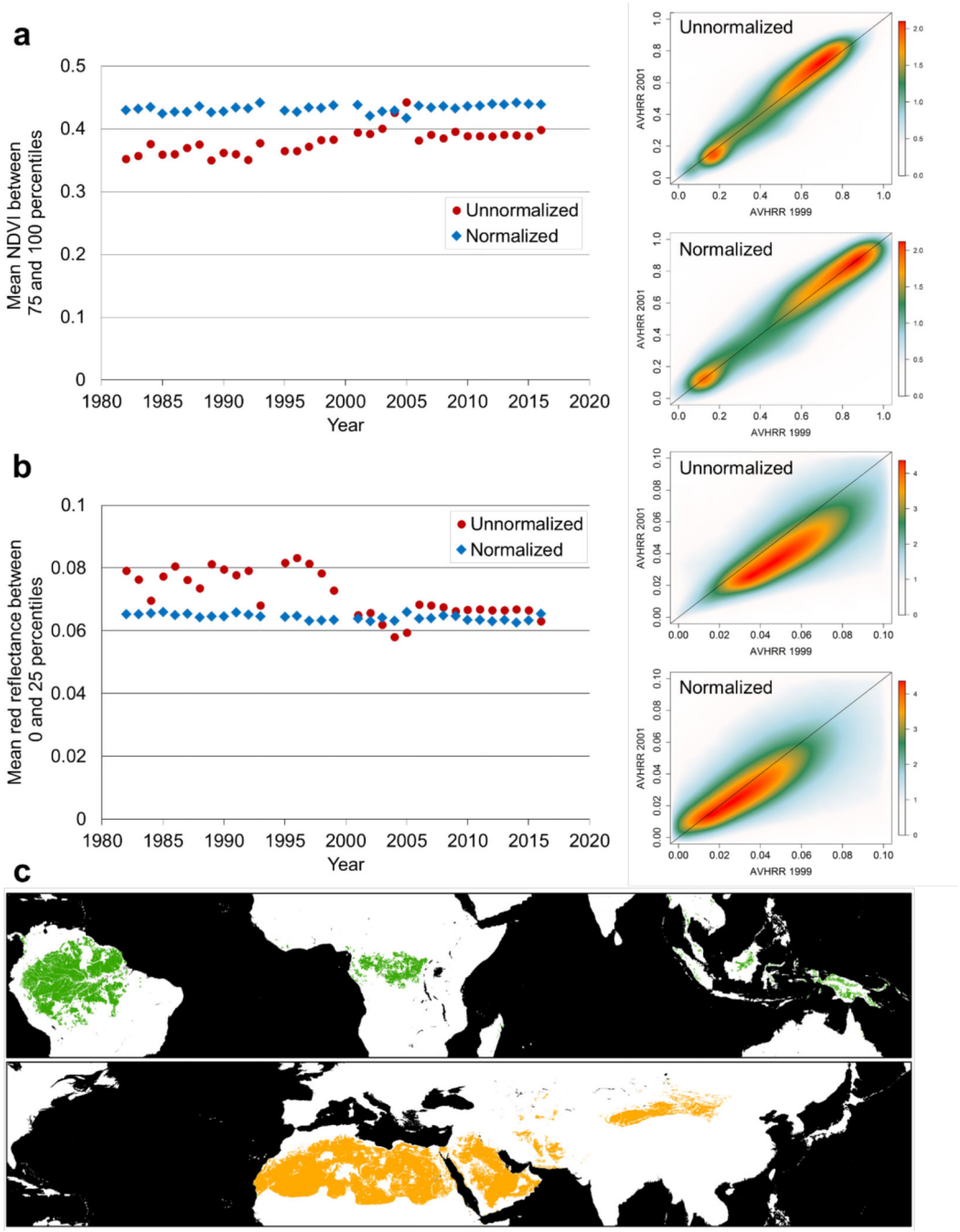

Extended Data Figure 6.

Adjusting systematic biases in annual AVHRR metrics using multi-year MODIS median as reference. The metric displayed in (**a**) is mean NDVI between 75 and 100 percentiles. This metric is related to the local peak growing season and was the most important variable driving the derived regression tree models for bare ground cover estimation. The metric displayed in (**b**) is mean red reflectance between 0 and 25 percentiles. This metric is also related to the local peak growing season and was the most important variable for tree cover estimation. For both (**a)** and (**b)**, the dot plots on the left show the normalized and

NASA Author Manuscript NASA Author Manuscript NASA Author Manuscript

unnormalized, annual, global mean values, excluding Antarctica and Greenland, and the density scatter plots on the right show pixel-level comparison between years 1999 and 2001 before (upper figure) and after normalization (lower figure). Normalizing AVHRR using MODIS as reference not only changes the absolute value and data range of each individual year, but also enhances year-to-year consistency. **c,** Maps of the intact forest landscape (upper figure, green) and deserts (lower figure, orange) that are used as stable targets for normalization.

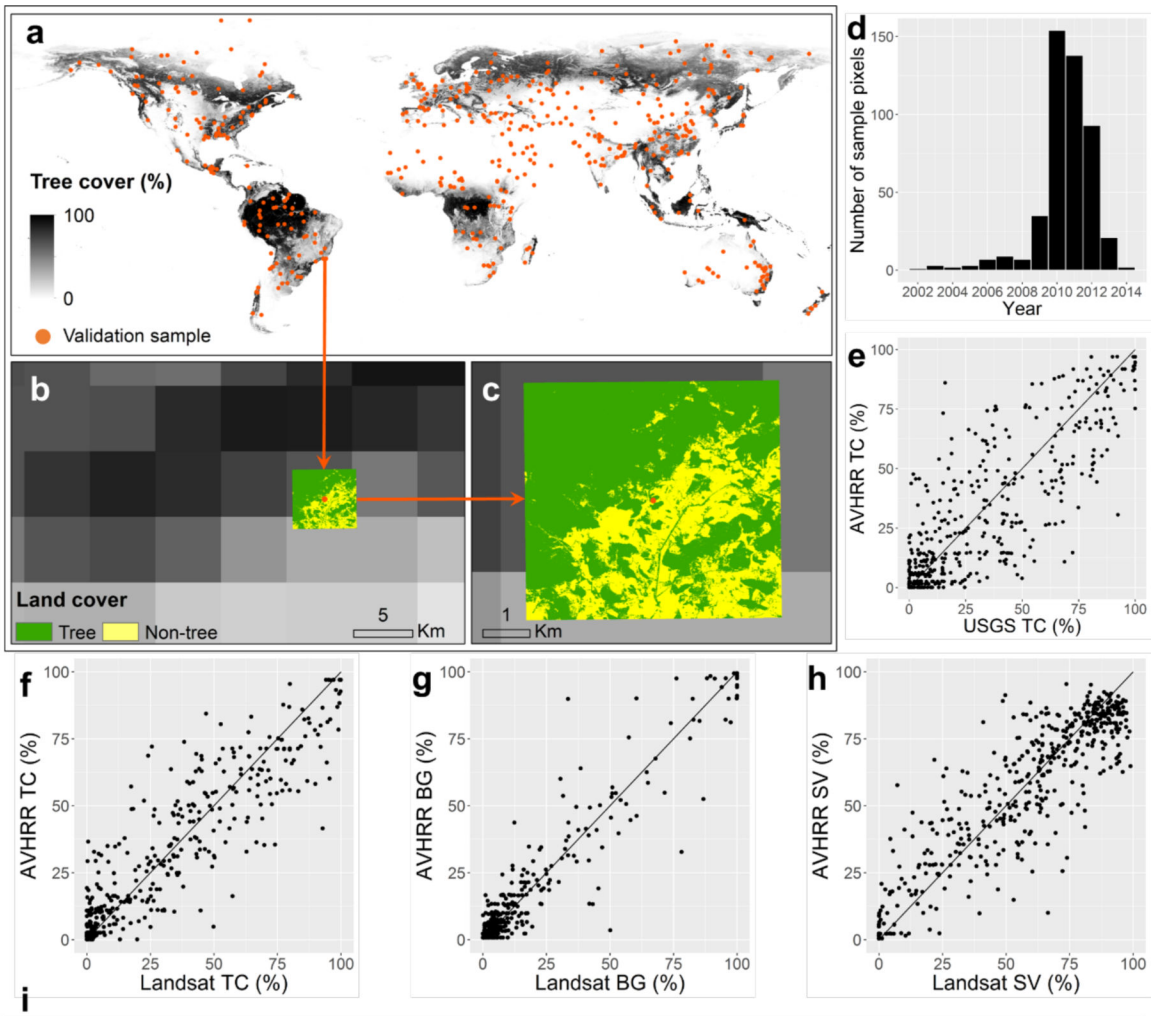

Products	Class	User's accuracy % (SE)	Producer's accuracy % (SE)	Overall accuracy % (SE)	RMSE % (SE)	MAE % (SE)	ME % (SE)	r^2
AVHRR TC vs USGS TC	TC	84 (2)	79 (1)	90.1 (0.6)	15.6 (5.0)	9.9 (0.6)	-1.5 (0.8)	0.73
	Not TC	92 (1)	94 (1)					
AVHRR TC vs Landsat TC	TC	85 (1)	88 (1)	93.4 (0.4)	11.2 (3.9)	6.6 (0.4)	1.0 (0.5)	0.85
	Not TC	96 (1)	95 (1)					
AVHRR BG vs Landsat BG	BG	91 (2)	92 (1)	95.6 (0.5)	9.1 (5.1)	4.4 (0.5)	0.4 (0.7)	0.93
	Not BG	97 (1)	97 (1)					
AVHRR SV vs Landsat SV	SV	91 (1)	90 (1)	90.4 (0.6)	14.0 (5.4)	9.6 (0.6)	-0.5 (0.8)	0.79
	Not SV	90 (1)	91 (1)					

Extended Data Figure 7.

NASA Author Manuscript NASA Author Manuscript NASA Author Manuscript

Accuracy assessment of AVHRR tree canopy (TC) cover, bare ground (BG) cover and short vegetation (SV) cover, based on a validation sample of 475 AVHRR pixels. **a**, Spatial distribution of the validation sample (red dot) overlaid on long-term (1982–2016) mean tree cover. The USGS tree cover reference data (5-km × 5-km, Universal Transverse Mercator projection) have greater spatial details (colored squares in **b** and **c**) due to their sub-meter resolution but have geolocation mismatch with the AVHRR product (0.05° × 0.05°, gray-scale squares in **b** and **c**) due to different projections. **d,** Temporal distribution of the USGS tree cover sample. **e,** Scatter plots of AVHRR tree cover against USGS reference tree cover. AVHRR and reference are matched by year and center coordinates. **f-h**, Scatter plots of AVHRR TC, BG and SV (year 2001) against Landsat-based estimates, which are free from geolocation mismatch. **i**, Quantitative error metrics, including conventional confusion matrices as well as root-meansquare-error (RMSE), mean absolute error (MAE), mean error (ME) and r^2. The standard error (SE) for the estimated error metrics is provided in the parentheses.

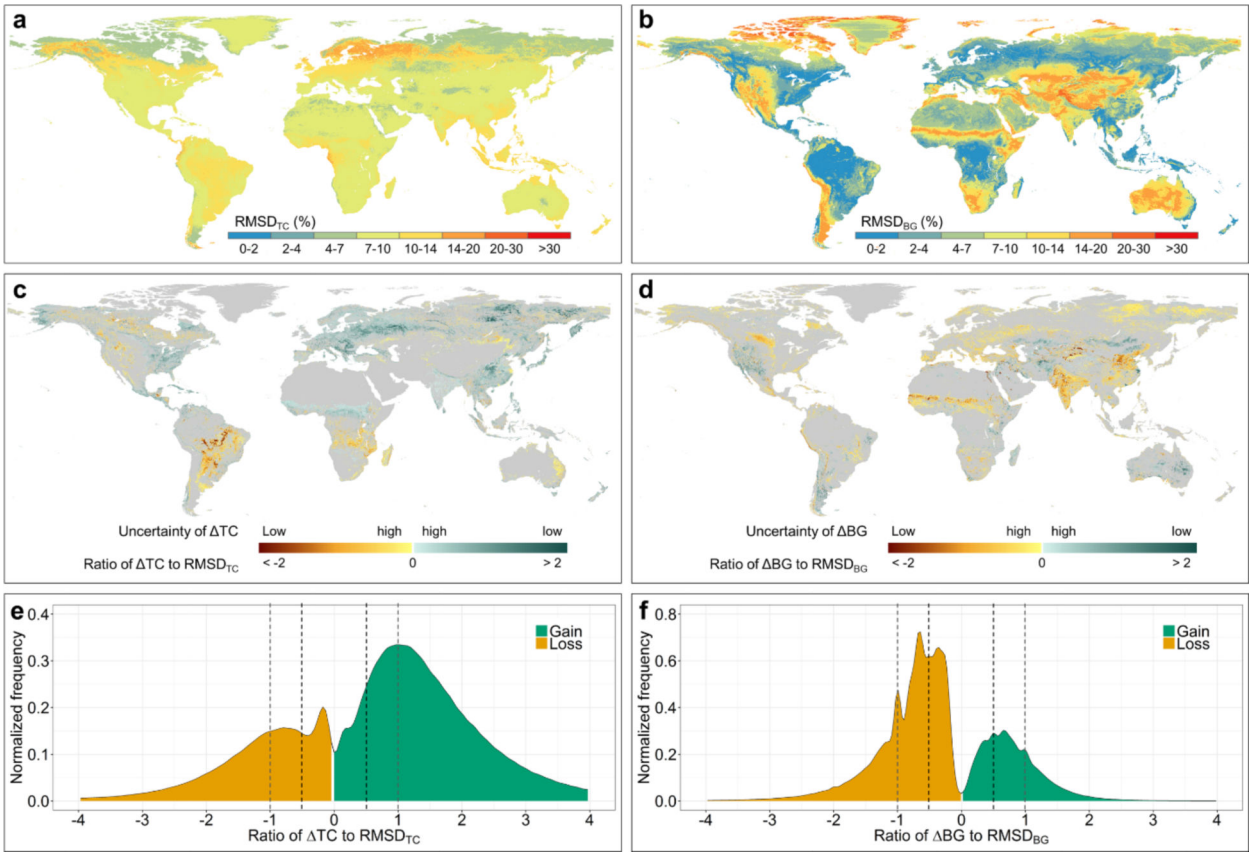

Extended Data Figure 8.

Uncertainty of tree cover change (ΔTC) and bare ground change (ΔBG). **a**, Spatial distribution of annual mean root-mean-square-deviation (RMSD) of TC between 1982 and 2016. **b**, Spatial distribution of annual mean RMSD of BG between 1982 and 2016. **c**, Spatial distribution of ΔTC uncertainty. **d**, Spatial distribution of ΔBG uncertainty. **e**, Normalized frequency distribution of ΔTC uncertainty. **f**, Normalized frequency distribution of ΔBG uncertainty. TC, BG and associated RMSD are outputs of regression tree models.

Uncertainty is represented by the ratio of long-term TC (BG) change estimates to associated RMSD estimates. Positive values of the ratio metric represent uncertainty of gain and negative values represent uncertainty of loss. A greater absolute value indicates lower uncertainty and vice versa. Area under the frequency distribution equals 1. The frequency distributions suggest that tree cover gain exceeds tree cover loss and bare ground loss exceeds bare ground gain for any threshold level (e.g. dashed lines), hence the observed trends (net gain in tree cover and a net loss in bare ground cover over the study period) are valid.

NASA Author Manuscript NASA Author Manuscript NASA Author Manuscript

NASA Author Manuscript NASA Author Manuscript NASA Author Manuscript

Extended Data Table 1.

Estimates of 1982 land cover area, 1982–2016 annual net land-cover change and 1982–2016 gross land-cover change at continental and global scales (excluding Antarctica). Annual net land-cover change (slope) and 1982 land-cover area were estimated using Theil-Sen regression of time series of annual land-cover area per continent or over the globe. Lower and upper slopes represent the 90% confidence interval. Reported p-value is for the Mann-Kendall test for trend. Gross land-cover change was estimated based on per-pixel nonparametric trend analysis. Per-pixel loss and gain were summed to derive gross loss and gain at the aggregated scales.

	Tree canopy cover							Short vegetation cover							Bare ground cover						
		Annual net change				Gross change			Annual net change				Gross change			Annual net change				Gross change	
Continent	Area 1982 (10^3 km^2)	Slope (10^3 km^2 yr^{-1})	Lower (10^3 km^2 yr^{-1})	Upper (10^3 km^2 yr^{-1})	p	loss (10^3 km^2)	gain (10^3 km^2)	Area 1982 (10^3 km^2)	Slope (10^3 km^2 yr^{-1})	Lower (10^3 km^2 yr^{-1})	Upper (10^3 km^2 yr^{-1})	p	loss (10^3 km^2)	gain (10^3 km^2)	Area 1982 (10^3 km^2)	Slope (10^3 km^2 yr^{-1})	Lower (10^3 km^2 yr^{-1})	Upper (10^3 km^2 yr^{-1})	p	loss (10^3 km^2)	gain (10^3 km^2)
Africa	4672	−1.9	−7.6	3.6	0.609	−267	262	11653	14.8	6.5	23.2	0.016	−268	571	13413	−12.4	−19.9	−4.7	0.020	−371	105
Asia	8457	37.5	28.0	45.3	0.000	−178	1170	21774	−22.9	−34.5	−9.6	0.008 •	−1261	760	13926	−15.1	−23.1	−7.4	0.002	−798	358
Europe	2719	28.3	20.4	32.8	0.000	−17	758	6320	−22.0	−27.3	−14.7	0.000	−673	50	668	−4.3	−5.8	−2.6	0.000	−92	9
North America	5815	15.6	3.5	24.2	0.020	−205	583	12921	−12.7	−4.1	−2.2	0.031	−594	286	4847	−2.5	−7.3	2.2	0.363	−186	140
South America	8767	−14.1	−20.5	−7.4	0.001	−621	190	7165	14.8	8.1	21.0	0.002	−224	655	1717	1.9	−1.2	3.8	0.307	−92	102
Oceania	680	0.1	−1.4	1.7	0.887	−40	56	4600	−4.4	−12.1	3.4	0.349	−132	50	2772	5.2	−3.9	12.5	0.280	−35	113
Global	31628	66.0	27.3	100.5	0.008	−1331	3039	64539	−26.0	−64.8	15.2	0.244 •	−3170	2380	37412	−34.0	−52.3	−10.0	0.023	−1582	830

Nature. Author manuscript; available in PMC 2019 August 08.

NASA Author Manuscript NASA Author Manuscript NASA Author Manuscript

Nature. Author manuscript; available in PMC 2019 August 08.

Extended Data Table 2.

Estimates of 1982 land cover area, 1982–2016 annual net land-cover change and 1982–2016 gross land-cover change at biome and climate zone scales. Consistent with Extended Data Table 1, annual net land-cover change (slope) and 1982 land-cover area were estimated using Theil-Sen regression of time series of annual land-cover area per biome or climate zone. Lower and upper slopes represent the 90% confidence interval. Reported p-value is for the Mann-Kendall test for trend. Gross land-cover change was estimated based on per-pixel non-parametric trend analysis. Per-pixel loss and gain were summed to derive gross loss and gain at the aggregated scales. See Extended Data Fig. 2b for the geographical distribution of biomes.

	Tree canopy cover							Short vegetation cover							Bare ground cover						
		Annual net change				Gross change			Annual net change				Gross change			Annual net change				Gross change	
Biome / climate zone	Area 1982 (10^3 km^2)	Slope (10^3 km^2 yr^{-1})	Lower (10^3 km^2 yr^{-1})	Upper (10^3 km^2 yr^{-1})	p	loss (10^3 km^2)	gain (10^3 km^2)	Area 1982 (10^3 km^2)	Slope (10^3 km^2 yr^{-1})	Lower (10^3 km^2 yr^{-1})	Upper (10^3 km^2 yr^{-1})	p	loss (10^3 km^2)	gain (10^3 km^2)	Area 1982 (10^3 km^2)	Slope (10^3 km^2 yr^{-1})	Lower (10^3 km^2 yr^{-1})	Upper (10^3 km^2 yr^{-1})	p	loss (10^3 km^2)	gain (10^3 km^2)
Tropical rainforest	10519	−1.9	−4.4	1.6	0.443	−332	315	3721	2.1	−1.0	5.1	0.307	−292	326	236	−0.4	−0.7	−0.1	0.025	−19	15
Tropical moist deciduous forest	3569	−2.5	−8.5	2.2	0.460	−373	285	6912	5.8	0.3	10.9	0.078	−236	386	492	−2.2	−3.0	−1.3	0.001	−71	29
Tropical dry forest	1236	−2.8	−5.1	−1.1	0.018	−184	99	5386	7.2	4.0	10.2	0.001	−70	246	821	−3.8	−5.9	−1.9	0.010	−121	32
Tropical mountain system	1333	3.5	2.4	4.5	0.000	−23	118	2092	−1.4	−3.1	0.2	0.118	−106	65	1092	−1.7	−2.7	−0.9	0.002	−61	17
Tropical shrubland|	149	0.3	−0.2	0.7	0.349	−15	20	4010	12.3	6.8	18.5	0.001	−41	371	4137	−12.0	−19.0	−6.1	0.003	−379	43
Tropical desert	19	0.0	0.0	0.0	0.532	0	1	692	1.6	0.2	3.4	0.061	−31	87	10846	−1.5	−3.4	−0.1	0.057	−88	31
Tropical climate zone	16837	−4.1	−14.4	3.6	0.320	−927	837	22691	30.0	14.7	43.0	0.002	−775	1480	17617	−25.5	−34.7	−12.0	0.002	−740	167
Subtropical humid forest	1566	8.2	4.4	12.0	0.002	−48	268	2866	−7.3	−10.5	−3.7	0.003	−236	46	196	−0.7	−1.4	−0.3	0.012	−38	22
Subtropical mountain system	516	3.1	2.3	3.8	0.000	−20	116	2571	−2.8	−4.3	−1.2	0.008	−153	68	1756	0.0	−1.7	1.8	0.932	−79	79
Subtropical dry forest	198	1.6	0.9	2.3	0.001	−8	49	1107	0.2	−0.5	0.8	0.755	−37	33	266	−1.2	−1.9	−0.6	0.002	−45	10
Subtropical steppe	179	−0.8	−2.0	0.2	0.191	−27	12	2594	−1.4	−4.2	1.8	0.460	−84	64	2106	3.2	−0.9	6.7	0.201	−61	106
Subtropical desert	29	−0.2	−0.4	0.0	0.118	−3	2	2606	−4.4	−10.3	1.3	0.233	−128	45	4001	4.5	−1.3	10.6	0.233	−46	133
Subtropical climate zone	2453	12.1	6.5	16.8	0.004	−105	448	11741	−14.0	−23.1	−5.6	0.013	−639	257	8323	5.6	−6.8	17.0	0.443	−269	350
Temperate continental forest	2172	21.4	15.1	26.0	0.000	−11	591	4451	−17.9	−22.5	−11.3	0.000	−528	28	277	−2.7	−3.4	−2.2	0.000	−61	7
Temperate mountain system	1552	5.9	3.6	7.4	0.001	−53	198	3459	−2.0	−4.0	0.5	0.211	−213	172	2175	−2.9	−5.1	−1.1	0.023	−161	62
Temperate oceanic forest	551	3.8	2.1	5.3	0.001	−6	101	1162	−3.3	−4.9	−1.8	0.003	−92	8	61	−0.4	−0.5	−0.2	0.000	−8	2
Temperate steppe	320	2.2	0.1	3.4	0.069	−18	56	4191	−2.9	−6.7	0.0	0.105	−130	72	1338	2.3	−1.5	5.8	0.363	−86	108
Temperate desert	61	−0.1	−0.2	0.1	0.514	−5	4	1661	−0.3	−2.9	3.5	0.955	−101	135	3642	0.3	−3.6	3.1	0.887	−135	103
Temperate climate zone	4681	33.5	21.0	41.9	0.000	−92	951	14814	−24.3	−37.3	−12.2	0.006	−1064	414	7491	−4.3	−14.0	1.8	0.268	−451	282
Boreal coniferous forest	3938	13.6	6.7	18.7	0.003	−75	415	4239	−12.6	−17.1	−6.3	0.002	−369	71	205	−1.4	−1.8	−0.9	0.001	−23	2
Boreal mountain system	2035	6.6	3.9	9.9	0.005	−61	225	3909	−6.2	−8.8	−3.3	0.003	−193	64	341	−1.2	−1.7	−0.6	0.002	−33	11
Boreal tundra woodland	971	1.3	−1.5	3.7	0.363	−58	82	2723	−0.9	−2.9	1.2	0.478	−63	52	228	−0.7	−1.2	−0.2	0.044	−16	5
Boreal climate zone	6796	21.0	7.9	31.0	0.009	−194	723	10857	−20.3	−27.5	−11.7	0.002	−625	187	772	−3.4	−4.5	−2.2	0.001	−71	19
Polar	236	2.2	0.9	3.1	0.009	−7	55	4109	0.4	−1.3	2.1	0.712	−43	30	3080	−2.6	−3.6	−1.1	0.010	−41	8

NASA Author Manuscript NASA Author Manuscript NASA Author Manuscript

Supplementary Material

Refer to Web version on PubMed Central for supplementary material.

Acknowledgments:

This study was funded by the NASA Making Earth System Data Records for Use in Research Environments (MEaSUREs) program (NNX13AJ35A). We thank Tom Loveland, Bruce Pengra and Pontus Olofsson for making their tree cover validation data available. We thank Charlene Dimiceli for assistance on VCF development and Zhen Song for assistance on AVHRR calibration.

References

1. Turner BL, Lambin EF & Reenberg A The emergence of land change science for global environmental change and sustainability. Proc. Natl. Acad. Sci. USA 104, 20666–20671 (2007). [PubMed: 18093934]
2. Foley JA et al. Global consequences of land use. Science 309, 570–574 (2005). [PubMed: 16040698]
3. Le Quéré C et al. Global carbon budget 2016. Earth Syst. Sci. Data 8, 605–649 (2016).
4. Alkama R & Cescatti A Biophysical climate impacts of recent changes in global forest cover. Science 351, 600–604 (2016). [PubMed: 26912702]
5. FAO. Global Forest Resources Assessment 2015. (UN Food and Agriculture Organization, Rome, Italy, 2015).
6. Bonan GB & Doney SC Climate, ecosystems, and planetary futures: The challenge to predict life in Earth system models. Science 359, eaam8328 (2018). [PubMed: 29420265]
7. Steffen W, Grinevald J, Crutzen P & McNeill J The Anthropocene: Conceptual and historical perspectives. Philos. Trans. A Math. Phys. Eng. Sci 369, 842–867 (2011). [PubMed: 21282150]
8. Hansen MC et al. High-resolution global maps of 21st-centry forest cover change. Science 342, 850–853 (2013). [PubMed: 24233722]
9. Hansen MC, Stehman SV & Potapov PV Quantification of global gross forest cover loss. Proc. Natl. Acad. Sci. USA 107, 8650–8655 (2010). [PubMed: 20421467]
10. Feng M et al. Earth science data records of global forest cover and change: Assessment of accuracy in 1990, 2000, and 2005 epochs. Remote Sens. Environ 184, 73–85 (2016).
11. DeFries RS et al. Mapping the land surface for global atmosphere-biosphere models: Toward continuous distributions of vegetation's functional properties. J. Geophys. Res. 100, 20867–20882 (1995).
12. FAO. Global ecological zoning for the global forest resources assessment 2000. (UN Food and Agriculture Organization, Rome, Italy, 2001).
13. Lambin EF et al. The causes of land-use and land-cover change: Moving beyond the myths. Global Environ. Change 11, 261–269 (2001).
14. Gibbs HK et al. Tropical forests were the primary sources of new agricultural land in the 1980s and 1990s. Proc. Natl. Acad. Sci. USA 107, 16732–16737 (2010). [PubMed: 20807750]
15. Song X-P, Huang C, Saatchi SS, Hansen MC & Townshend JR Annual carbon emissions from deforestation in the Amazon basin between 2000 and 2010. PLoS One 10, e0126754 (2015). [PubMed: 25951328]
16. Margono BA, Potapov PV, Turubanova S, Stolle F & Hansen MC Primary forest cover loss in Indonesia over 2000–2012. Nat. Clim. Change 4, 730–735 (2014).
17. Ordway EM, Asner GP & Lambin EF Deforestation risk due to commodity crop expansion in sub-Saharan Africa. Environ. Res. Lett. 12, 044015 (2017).
18. Hicke JA et al. Postfire response of North American boreal forest net primary productivity analyzed with satellite observations. Glob. Change Biol. 9, 1145–1157 (2003).
19. van Mantgem PJ et al. Widespread increase of tree mortality rates in the western United States. Science 323, 521–524 (2009). [PubMed: 19164752]

NASA Author Manuscript NASA Author Manuscript NASA Author Manuscript

20. McManus KM et al. Satellite-based evidence for shrub and graminoid tundra expansion in northern Quebec from 1986 to 2010. Glob. Change Biol 18, 2313–2323 (2012).
21. Mitchard ET & Flintrop CM Woody encroachment and forest degradation in sub-Saharan Africa's woodlands and savannas 1982–2006. Philos. Trans. R. Soc. Lond., Ser. B: Biol. Sci 368, 20120406 (2013). [PubMed: 23878342]
22. Brandt M et al. Human population growth offsets climate-driven increase in woody vegetation in sub-Saharan Africa. Nat. Ecol. Evol 1, 0081 (2017).
23. Harsch MA, Hulme PE, McGlone MS & Duncan RP Are treelines advancing? A global meta-analysis of treeline response to climate warming. Ecol. Lett 12, 1040–1049 (2009). [PubMed: 19682007]
24. Potapov PV et al. Eastern Europe's forest cover dynamics from 1985 to 2012 quantified from the full Landsat archive. Remote Sens. Environ 159, 28–43 (2015).
25. Piao S et al. Detection and attribution of vegetation greening trend in China over the last 30 years. Glob Chang Biol 21, 1601–1609 (2015). [PubMed: 25369401]
26. Birdsey R, Pregitzer K & Lucier A Forest carbon management in the United States. J. Environ. Qual 35, 1461–1469 (2006). [PubMed: 16825466]
27. Donohue RJ, McVicar TR & Roderick ML Climate-related trends in Australian vegetation cover as inferred from satellite observations, 1981–2006. Glob. Change Biol 15, 1025–1039 (2009).
28. Liu YY et al. Changing climate and overgrazing are decimating Mongolian steppes. PLoS One 8, e57599 (2013). [PubMed: 23451249]
29. Herrick JE et al. National ecosystem assessments supported by scientific and local knowledge. Front. Ecol. Environ 8, 403–408 (2010).
30. Evenson RE & Gollin D Assessing the Impact of the Green Revolution, 1960 to 2000. Science 300, 758–762 (2003). [PubMed: 12730592]
31. Ying Q et al. Global bare ground gain from 2000 to 2012 using Landsat imagery. Remote Sens. Environ 194, 161–176 (2017).
32. Myneni RB, Keeling CD, Tucker CJ, Asrar G & Nemani RR Increased plant growth in the northern high latitudes from 1981 to 1991. Nature 386, 698–702 (1997).
33. Forkel M et al. Codominant water control on global interannual variability and trends in land surface phenology and greenness. Glob. Chang Biol 21, 3414–3435 (2015). [PubMed: 25882036]
34. Zhu Z et al. Greening of the Earth and its drivers. Nat. Clim. Change 6, 791–795 (2016).
35. Mao J et al. Human-induced greening of the northern extratropical land surface. Nat. Clim. Change 6, 959–963 (2016).
36. Pan Y et al. A large and persistent carbon sink in the world's forests. Science 333, 988–993 (2011). [PubMed: 21764754]
37. DeFries RS, Townshend JRG & Hansen MC Continuous fields of vegetation characteristics at the global scale at 1-km resolution. J. Geophys. Res 104, 16911–16923 (1999).
38. Hansen MC et al. Global percent tree cover at a spatial resolution of 500 meters: First results of the MODIS vegetation continuous fields algorithm. Earth Interact. 7, 10 (2003).
39. Hansen MC et al. Towards an operational MODIS continuous field of percent tree cover algorithm: examples using AVHRR and MODIS data. Remote Sens. Environ. 83, 303–319 (2002).
40. Hansen MC, Townshend JRG, DeFries RS & Carroll M Estimation of tree cover using MODIS data at global, continental and regional/local scales. Int. J. Remote Sens 26, 4359–4380 (2005).
41. Hansen MC et al. Continuous fields of land cover for the conterminous United States using Landsat data: First results from the Web-Enabled Landsat Data (WELD) project. Remote Sens. Lett. 2, 279–288 (2011).
42. Jennings SB, Brown ND & Sheil D Assessing forest canopies and understorey illumination: Canopy closure, canopy cover and other measures. Forestry 72, 59–74 (1999).
43. Korhonen L, Korhonen KT, Rautiainen M & Stenberg P Estimation of forest canopy cover : A comparison of field measurement techniques. Silva Fenn. 40, 577–588 (2006).
44. Hansen MC et al. Monitoring conterminous United States (CONUS) land cover change with web-enabled Landsat data (WELD). Remote Sens. Environ. 140, 466–484 (2014).

NASA Author Manuscript NASA Author Manuscript NASA Author Manuscript

45. Pinzon J & Tucker C A non-stationary 1981–2012 AVHRR NDVI3g time series. Remote Sens. 6, 6929–6960 (2014).
46. Tucker C et al. An extended AVHRR 8-km NDVI dataset compatible with MODIS and SPOT vegetation NDVI data. Int. J. Remote Sens 26, 4485–4498 (2005).
47. Franch B et al. A 30+ year AVHRR land surface reflectance climate data record and its application to wheat yield monitoring. Remote Sens. 9, 296 (2017).
48. Pedelty J et al. Generating a long-term land data record from the AVHRR and MODIS Instruments. IEEE Int. Geosci. Remote Sens. Symp. Proc, 1021–1025 (2007).
49. Tucker CJ Red and photographic infrared linear combinations for monitoring vegetation. Remote Sens. Environ. 8, 127–150 (1979).
50. Holben BN Characteristics of maximum-value composite images from temporal AVHRR data. Int. J. Remote Sens 7, 1417–1434 (1986).
51. Loveland TR et al. Development of a global land cover characteristics database and IGBP DISCover from 1 km AVHRR data. Int. J. Remote Sens 21, 1303–1330 (2000).
52. Hansen MC, DeFries RS, Townshend JRG & Sohlberg RA Global land cover classification at 1 km spatial resolution using a classification tree approach. Int. J. Remote Sens 21, 1331–1364 (2000).
53. DeFries RS, Hansen M, Townshend JRG & Sohlberg R Global land cover classifications at 8 km spatial resolution: The use of training data derived from Landsat imagery in decision tree classifiers. Int. J. Remote Sens 19, 3141–3168 (1998).
54. Bartholomé E & Belward AS GLC2000: A new approach to global land cover mapping from Earth observation data. Int. J. Remote Sens 26, 1959–1977 (2005).
55. Lloyd D A phenological classification of terrestrial vegetation cover using shortwave vegetation index imagery. Int. J. Remote Sens 11, 2269–2279 (1990).
56. Reed BC et al. Measuring phenological variability from satellite imagery. J. Veg. Sci 5, 703–714 (1994).
57. DeFries R, Hansen M & Townshend J Global discrimination of land cover types from metrics derived from AVHRR pathfinder data. Remote Sens. Environ 54, 209–222 (1995).
58. Latifovic R, Pouliot D & Dillabaugh C Identification and correction of systematic error in NOAA AVHRR long-term satellite data record. Remote Sens. Environ 127, 8497 (2012).
59. Kaufmann RK et al. Effect of orbital drift and sensor changes on the time series of AVHRR vegetation index data. IEEE Trans. Geosci. Remote Sens. 38, 2584–2597 (2000).
60. Kaufman YJ & Holben BN Calibration of the AVHRR visible and near-IR bands by atmospheric scattering, ocean glint and desert reflection. Int. J. Remote Sens 14, 21–52 (1993).
61. Vermote E & Kaufman YJ Absolute calibration of AVHRR visible and near-infrared channels using ocean and cloud views. Int. J. Remote Sens 16, 2317–2340 (1995).
62. Los SO Estimation of the ratio of sensor degradation between NOAA AVHRR channels 1 and 2 from monthly NDVI composites. IEEE Trans. Geosci. Remote Sens 36, 206–213 (1998).
63. Myneni RB, Tucker CJ, Asrar G & Keeling CD Interannual variations in satellite-sensed vegetation index data from 1981 to 1991. J. Geophys. Res. Atmos 103, 6145–6160 (1998).
64. Gutman GG On the use of long-term global data of land reflectances and vegetation indices derived from the advanced very high resolution radiometer. J. Geophys. Res. Atmos 104, 6241–6255 (1999).
65. Donohue RJ, Roderick ML & McVicar TR Deriving consistent long-term vegetation information from AVHRR reflectance data using a cover-triangle-based framework. Remote Sens. Environ 112, 2938–2949 (2008).
66. Hansen MC et al. A method for integrating MODIS and Landsat data for systematic monitoring of forest cover and change in the Congo basin. Remote Sens. Environ 112, 2495–2513 (2008).
67. Potapov PV et al. Quantifying forest cover loss in Democratic Republic of the Congo, 2000–2010, with Landsat ETM+ data. Remote Sens. Environ 122, 106–116 (2012).
68. Chavez PS, Jr Radiometric calibration of Landsat Thematic Mapper multispectral images. Photogramm. Eng. Remote Sensing 55, 1285–1294 (1989).

NASA Author Manuscript NASA Author Manuscript NASA Author Manuscript

69. Song. C, Woodcock CE, Seto KC, Lenney MP & Macomber SA Classification and change detection using Landsat TM data: When and how to correct atmospheric effects? Remote Sens. Environ 75, 230–244 (2001).
70. Woodcock CE, Macomber SA, Pax-Lenney M & Cohen WB Monitoring large areas for forest change using Landsat: Generalization across space, time and Landsat sensors. Remote Sens. Environ. 78, 194–203 (2001).
71. Potapov P et al. The last frontiers of wilderness: Tracking loss of intact forest landscapes from 2000 to 2013. Sci. Adv 3, e1600821 (2017). [PubMed: 28097216]
72. Breiman L, Friedman JH, Olshen RA & Stone CJ Classification and regression trees. (Chapman & Hall/CRC, 1984).
73. Hansen M, Dubayah R & Defries R Classification trees: An alternative to traditional land cover classifiers. Remote Sens. Lett 17, 1075–1081 (1996).
74. Friedl MA & Brodley CE Decision tree classification of land cover from remotely sensed data. Remote Sens. Environ 61, 399–409 (1997).
75. Mascorro VS, Coops NC, Kurz WA & Olguin M Choice of satellite imagery and attribution of changes to disturbance type strongly affects forest carbon balance estimates. Carbon Balance Manag. 10, 30 (2015). [PubMed: 26705411]
76. Strahler AH et al. Global land cover validation: recommendations for evaluation and accuracy assessment of global land cover maps. (Office for Official Publications of the European Communities, Luxembourg, 2006).
77. Olofsson P et al. A global land-cover validation data set, part I: Fundamental design principles. Int. J. Remote Sens 33, 5768–5788 (2012).
78. Stehman SV, Olofsson P, Woodcock CE, Herold M & Friedl MA A global land-cover validation data set, II: Augmenting a stratified sampling design to estimate accuracy by region and land-cover class. Int. J. Remote Sens 33, 6975–6993 (2012).
79. Pengra B, Long J, Dahal D, Stehman SV & Loveland TR A global reference database from very high resolution commercial satellite data and methodology for application to Landsat derived 30m continuous field tree cover data. Remote Sens. Environ. 165, 234–248 (2015).
80. Willmott CJ Some comments on the evaluation of model performance. Bull. Am. Meteorol. Soc 63, 1309–1313 (1982).
81. Cochran WG Sampling Techniques (3rd edition). (John Wiley & Sons, 1977).
82. Sen PK Estimates of the regression coefficient based on Kendall's tau. J. Am. Stat. Assoc 63, 1379–1389 (1968).
83. Mann HB Nonparametric tests against trend. Econometrica 13, 245–259 (1945).
84. Guay KC et al. Vegetation productivity patterns at high northern latitudes: A multi-sensor satellite data assessment. Glob. Change Biol. 20, 3147–3158 (2014).
85. Fensholt R et al. Greenness in semi-arid areas across the globe 1981–2007 — an Earth observing satellite based analysis of trends and drivers. Remote Sens. Environ 121, 144–158 (2012).
86. Andela N, Liu YY, van Dijk AIJM, de Jeu RAM & McVicar TR Global changes in dryland vegetation dynamics (1988–2008) assessed by satellite remote sensing: comparing a new passive microwave vegetation density record with reflective greenness data. Biogeosciences 10, 6657–6676 (2013).
87. Geist HJ & Lambin EF Proximate Causes and Underlying Driving Forces of Tropical Deforestation. Bioscience 52, 143–150 (2002).
88. DeFries RS, Rudel T, Uriarte M & Hansen M Deforestation driven by urban population growth and agricultural trade in the twenty-first century. Nat. Geosci. 3, 178–181 (2010).
89. Liu S et al. Grand Challenges in Understanding the Interplay of Climate and Land Changes. Earth Interact 21, 1–43 (2017).
90. De Sy V et al. Land use patterns and related carbon losses following deforestation in South America. Environ. Res. Lett 10, 124004 (2015).
91. Tyukavina A et al. Types and rates of forest disturbance in Brazilian Legal Amazon, 2000–2013. Sci. Adv 3, e1601047 (2017). [PubMed: 28439536]
92. Breiman L Bagging Predictors. Mach. Learn. 24, 123–140 (1996).

93. Gessner U, Machwitz M, Conrad C & Dech S Estimating the fractional cover of growth forms and bare surface in savannas. A multi-resolution approach based on regression tree ensembles. Remote Sens. Environ. 129, 90–102 (2013).

NASA Author Manuscript

NASA Author Manuscript

NASA Author Manuscript

NASA Author Manuscript

NASA Author Manuscript

NASA Author Manuscript

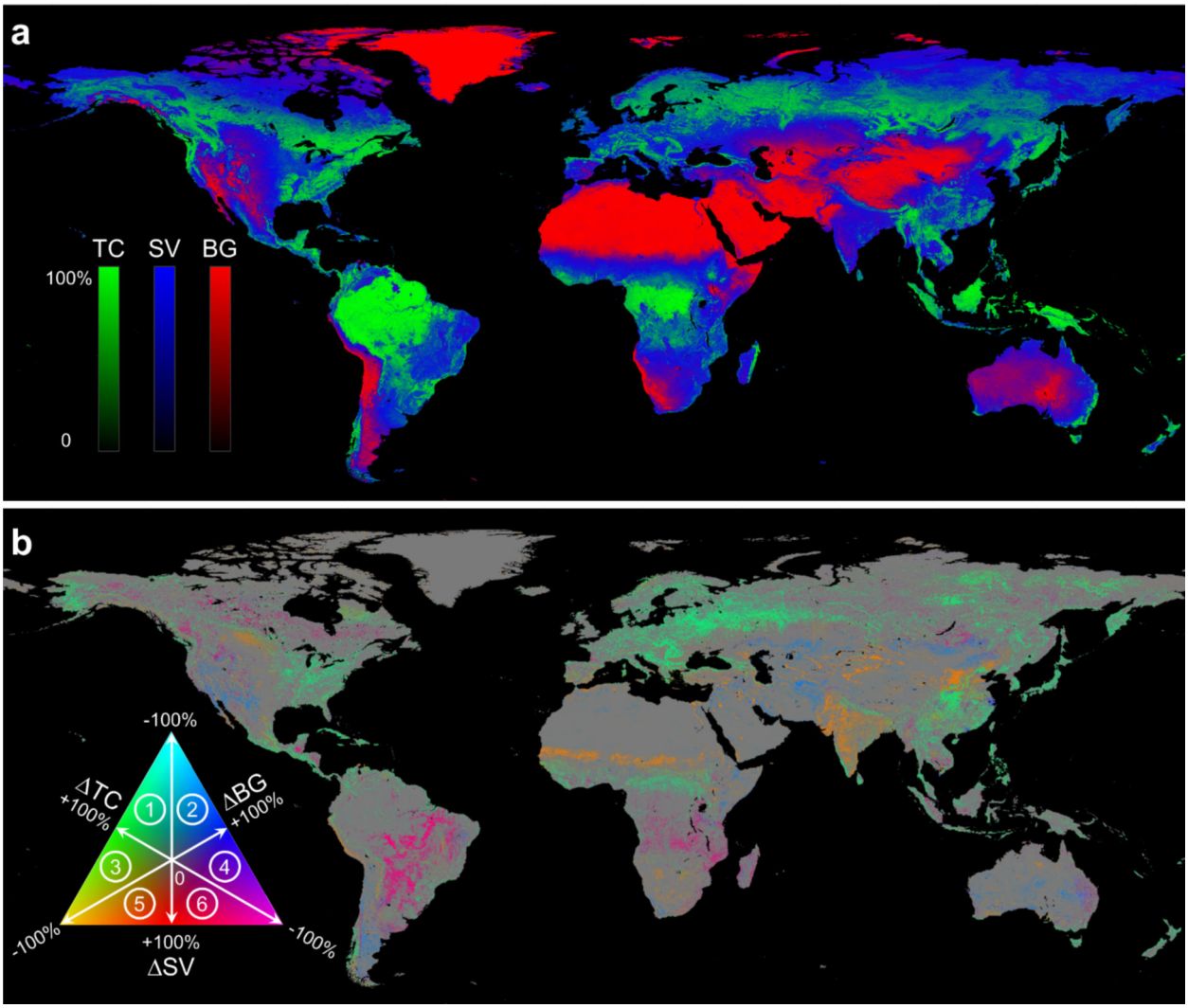

Figure 1.

A satellite-based record of global tree canopy (TC) cover, short vegetation (SV) cover and bare ground (BG) cover between 1982 and 2016. **a**, Mean annual estimates. **b,** Long-term change estimates. Both mean and change estimates are expressed as percent of pixel area at 0.05° × 0.05° spatial resolution. Pixels showing a statistically significant trend (Mann-Kendall test, $p < 0.05$) in either TC, SV or BG are depicted on the change map. Circled numbers in the color legend denote dominant change directions: 1: ΔTC+ with ΔSV-; 2: ΔBG+ with ΔSV-; 3: ΔTC+ with ΔBG-; 4: ΔBG+ with ΔTC-; 5: ΔSV+ with ΔBG- and 6: ΔSV+ with ΔTC-.

NASA Author Manuscript

NASA Author Manuscript

NASA Author Manuscript

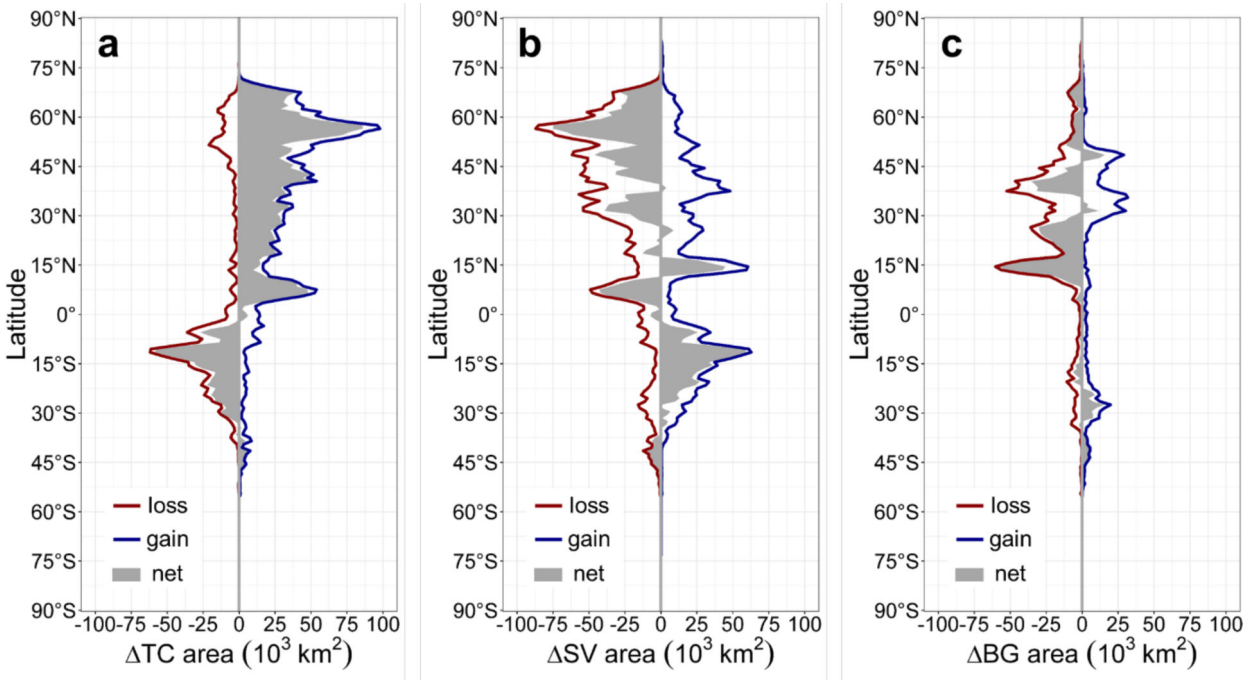

Figure 2.

Latitudinal profiles of land cover change between 1982 and 2016. **a**, tree canopy cover change (ΔTC). **b**, short vegetation cover change (ΔSV). **c**, bare ground cover change (ΔBG). Area statistics were calculated for every 1° latitude.

NASA Author Manuscript
NASA Author Manuscript
NASA Author Manuscript

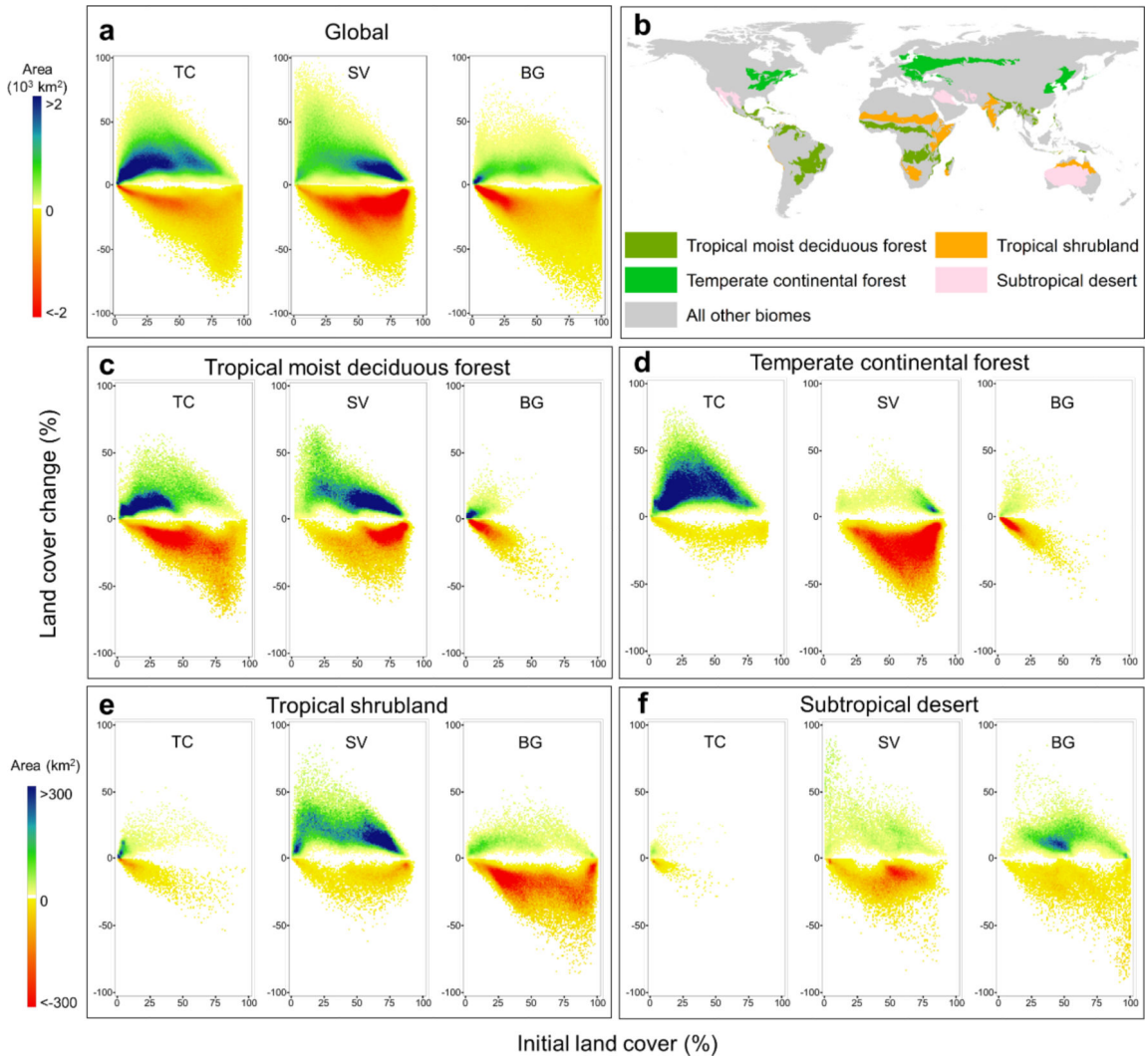

Figure 3.

Intensity plots of gross loss and gain area in tree canopy (TC) cover, short vegetation (SV) cover and bare ground (BG) cover during 1982–2016. **a,** Global-scale plots (upper-left color bar). Initial land cover (x-axis) is defined as mean value of the first five years 1982–1986. To create these plots, for each cover class, percent change layer (Fig. 1b) and initial cover layer are used to construct a 2D histogram with bin size of 1% for both axes. Then, total change area in each bin is calculated and plotted. Data points located towards the lower-right corner of the TC plot are more likely to be deforestation (that is, points with large initial tree cover and large reduction in tree cover). The concentrated blue region of the SV plots reflects cropland intensification. The green belt on the BG plot suggests that vegetation loss occurred across the entire range of BG coverage. The dominance of TC gain over TC loss, SV loss over SV gain and BG loss over BG gain are also clearly revealed; **b,** Geographical distribution of four highlighted biomes[12] with largest gross areal changes; **c,** largest gross TC loss and SV gain; **d,** largest gross TC gain and SV loss; **e,** largest gross BG loss; **f,** largest gross BG gain. The lower-left color bar is consistent across biomes (**c-f**) and cover types. Long-term gross dynamics of TC, SV and BG changes vary considerably between

biomes. See Extended Data Fig. 2 for other biomes and Extended Data Table 2 for change area estimates.

NASA Author Manuscript

NASA Author Manuscript

NASA Author Manuscript

NASA Author Manuscript

NASA Author Manuscript

NASA Author Manuscript

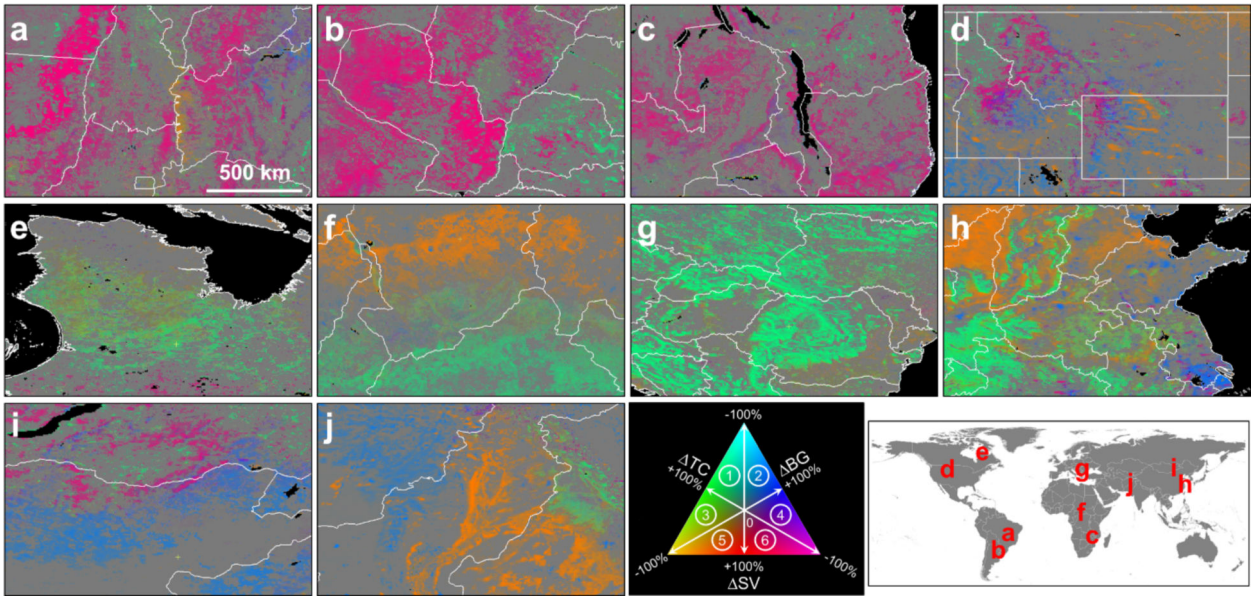

Figure 4.

Regional subsets of changes in tree canopy (TC) cover, short vegetation (SV) cover and bare ground (BG) cover. **a,** Cerrado ecoregion in Brazil, centered at (11.4°S, 46.5°W). **b**, Gran Chaco ecoregion in Bolivia, Argentina and Paraguay, centered at (22.5°S, 55.7°W). **c,** Miombo woodlands in southeast Africa, centered at (12.4°S, 33.9°E). **d,** Western United States, centered at (44.5°N, 110.0°W). **e,** Quebec, Canada, centered at (57.9°N, 71.6°W). **f,** Central Africa, centered at (10.4°N, 19.4°E). **g,** Eastern Europe, centered at (46.1°N, 20.3°E). **h,** Eastern China, centered at (35.0°N, 115.1°E). **i,** Eastern Mongolia, centered at (48.7°N, 111.0°E). **j,** Afghanistan and Pakistan, centered at (30.7°N, 70.6°E). Circled numbers in the color legend denote dominant change directions: 1: ΔTC+ with ΔSV-; 2: ΔBG+ with ΔSV-; 3: ΔTC+ with ΔBG-; 4: ΔBG+ with ΔTC-; 5: ΔSV+ with ΔBG- and 6: ΔSV+ with ΔTC-.